NON-DESTRUCTIVE CHARACTERIZATION OF PRINTED HYDROGEL SCAFFOLDS USING SYNCHROTRON-BASED IMAGING

A Thesis Submitted to the
College of Graduate and Postdoctoral Studies
in Partial Fulfillment of the Requirements
for the Degree of Master of Science
in the Division of Biomedical Engineering
University of Saskatchewan
Saskatoon

By

Subashree Srinivasan

© Copyright Subashree Srinivasan, June 2020. All rights reserved.

PERMISSION TO USE

In presenting this thesis in partial fulfillment of the requirements for a Master of Science degree from the University of Saskatchewan, I agree that the Libraries of this University may make it freely available for inspection. I further agree that permission for copying of this thesis in any manner, in whole or in part, for scholarly purposes may be granted by Dr. Daniel Chen and Dr. Ning Zhu who supervised my thesis work or, in their absence, by the Head of the Department or the Dean of the College in which my thesis work was done. It is understood that any copying or publication or use of this thesis or parts thereof for financial gain shall not be allowed without my written permission. It is also understood that due recognition shall be given to me and to the University of Saskatchewan in any scholarly use, which may be made of any material in my thesis.

Requests for permission to copy or to make other uses of materials in this thesis/dissertation in whole or part should be addressed to:

Head of the Division of Biomedical Engineering

57 Campus Drive, University of Saskatchewan

Saskatoon, Saskatchewan S7N 5A9

Canada

OR

Dean

College of Graduate and Postdoctoral Studies

University of Saskatchewan

116 Thorvaldson Building, 110 Science Place

Saskatoon, Saskatchewan S7N 5C9

Canada

ABSTRACT

Hydrogel scaffolds have shown great promise as main components in the artificial tissue-engineered scaffolds for the repair of injured tissues. The fabrication of hydrogel scaffolds with precise geometry can be achieved by three-dimension (3D) printing (also known as additive manufacturing) technology. One of the key requirements in 3D printing of hydrogels is to achieve high fidelity or printability to fabricate the scaffolds that can resemble the designed structure. For the printability characterization, non-destructive visualization of 3D printed scaffolds is essentially needed. Also, the 3D printed scaffolds, when implanted *in vivo*, need to be visualized for tracking their success, which may include the scaffold status such as mechanical deformation and formation of new tissues. Hence, 3D visualization of the hydrogel scaffold structure is vital to characterize the printability and scaffold status. Unfortunately, conventional imaging techniques in tissue engineering are impossible to non-destructively visualize the whole 3D structure of hydrogel scaffolds due to the limited imaging capability. To address these issues mentioned, the aim of this research is to 1) study synchrotron propagation-based imaging technique with computed tomography (SR-PBI-CT) imaging parameters to visualize the printed scaffolds non-destructively, 2) 3D print the gelatin methacrylate (GelMA) hydrogel scaffolds, and non-destructively characterize the printed scaffolds printability and mechanical deformation using the optimal SR-PBI-CT imaging method.

The SR-PBI-CT imaging parameters were examined using a standard sample alginate scaffold and found optimal Sample to Detector Distance (SDD), X-ray energy, and the number of projections to visualize printed hydrogel scaffolds. Upon finding optimal SR-PBI-CT imaging parameters, the characterization of printability and mechanical deformation of printed GelMA scaffolds was conducted based on the imaging results. The hydrogels were clearly visualized and characterized from the phase-retrieved reconstructed slices. From the phase-retrieved reconstructed slices, the printability results show the best printing speed for printing GelMA scaffolds, and the compression study shows the strength and status of the printed scaffold under different levels of deformation. The results of the printability and mechanical deformation characterization can be used to improve the design and fabrication of GelMA scaffolds. This study illustrates that SR-PBI-CT is feasible for non-destructive visualization of the hydrogel scaffolds as well as the quantification of their structures.

The contribution of this research also rests on determining the optimal imaging setup or parameters for hydrogel scanning using SR-PBI-CT. Also, this research illustrates it is feasible to lower the X-ray dose during the imaging by reducing the number of projections from 1800 to 450, thus reducing the radiation exposure by 75% to the imaged samples. This would represent a significant step towards the application of the SR-PBI-CT to visualize hydrogel scaffolds implanted in living animal models and eventually to human patients.

ACKNOWLEDGMENTS

I would like to express my sincere and deepest gratitude to my supervisors, Prof. Daniel Chen and Prof. Ning Zhu, for their great support, encouragement, guidance during my academic studies and research. They have been a great source of knowledge and inspired me to pursue this research. I would like to thank my advisory committee members, Prof. Chris Zhang and Prof. Tate Cao, for their valuable comments and suggestions.

I gratefully acknowledge the financial support from the NSERC Discovery Grant to Prof. Chen and Prof. Zhu.

I acknowledge, major parts of the research described in this thesis was performed at the Canadian Light Source, a national research facility of the University of Saskatchewan, which is supported by the Canada Foundation for Innovation (CFI), the Natural Sciences and Engineering Research Council (NSERC), the National Research Council (NRC), the Canadian Institutes of Health Research (CIHR), the Government of Saskatchewan, and the University of Saskatchewan. I would like to thank Dr. Sergey Gasilov (BMIT beamline responsible) for providing sufficient time and support to perform experiments at CLS.

I would like to thank Dr. Liqun Ning for his committed tutoring during academic studies. The technical support from Mr. Doug Bitner, Mr. Nanfang Zhao and Mr. Rob Peace is highly appreciated. I appreciate Dr. Adam McInnes for his support throughout my academic studies. My sincere thanks to all friends from Biofabrication Laboratory who have been a great support during my academic studies and research. I am grateful for the motivation and support from Dr. Chithra Karunakaran (Canadian Light Source), Dr. Gurubalan Annadurai and Mrs. Pavithra Pachamuthu. I always extend my gratitude to Rajan and Selvi for their love and support. I thank Adarsh for his friendly support.

Finally, above all, I am grateful to my parents, Srinivasan and Hemamalini, for their love, patience, and motivation. My deepest thanks to my sister Snehalathaa for her encouragement and support.

TABLE OF CONTENTS

LIST OF FIGURES

LIST OF TABLES

LIST OF ABBREVIATIONS

μCT:	X-ray micro-computed tomography
3D:	Three dimensional
ABI:	Analyzer-based imaging
ACI:	Absorption contrast imaging
BMIT:	Bio-Medical Imaging and Therapy
CLS:	Canadian Light Source
CLSM:	Confocal laser scanning microscopy
CNR:	Contrast-to-noise ratio
CT:	Computed tomography
DEI:	Diffraction enhanced imaging
DPBS:	Dulbecco's phosphate-buffered saline
ECM:	Extracellular matrix
EBB:	Extrusion-based bioprinting
GelMA:	Gelatin methacrylate
KES:	K-edge subtraction
MRI:	Magnetic resonance imaging
NFI:	Near field imaging
PBI:	Propagation-based imaging
PBS:	Phosphate-buffered saline
PCI:	Phase contrast imaging
PEG:	Polyethylene glycol
PPI:	Phase propagation imaging
SDD:	Sample-to-detector distance
SEM:	Scanning electron microscope
SR-PBI:	Synchrotron radiation propagation-based imaging technique
SR-PBI-CT:	Synchrotron radiation propagation-based imaging technique with computed tomography
TEM:	Transmission electron microscope
TERM:	Tissue engineering and regenerative medicine

TIE:	Transport-of-intensity equation
UFO:	Ultra-Fast-Online software (an open-source package)
USI:	Ultrasound imaging
UV:	Ultraviolet

CHAPTER 1. INTRODUCTION

1.1. Background

Tissue engineering organizes biomaterials, nanoparticles, drugs, and biological molecules such as cells, growth factors, and genes together to provide cure to the damaged tissues or replace the dead tissues in patients [1,2]. Research in regenerative medicine, of which tissue engineering is a part, is aimed at restoring, maintaining, and improving tissue functions. The tissue engineering approaches to the development of new tissues or the repair of damaged organs can be understood through the following principle (Figure 1.1), which involves a) isolation of tissue-specific cells; b) cell seedling into the developed hydrogel scaffolds; c) maturation of cells in *in vitro* [2,3]. By the three methods mentioned above, tissue engineering plays a vital role in tissue regeneration and repair with scaffolds (generally highly porous in structure), with these scaffolds contributing to the development of new tissues by acting as a supportive and sacrificial platform [4]. Also, it surpasses the limitations of organ donation shortages and reducing the immunological rejections after transplantation by the effective utilization of biomaterials [5]. As the biocompatible materials, hydrogels have been extensively used to load cells for tissue engineering applications [6,7]. Due to their superiority of providing a biocompatible, tissue-like environment for maintaining cellular functions such as viability, proliferation and migration, hydrogel-based tissue scaffolds are widely used in tissue regeneration. 3D hydrogels intently take after some fundamental features of local extracellular matrices (ECM), supporting excellent cell proliferation, viability, and physiology [8].

3D printing of hydrogels allows for highly precise control of internal hydrogel structure, pore size, and external geometry. This is often superior to other conventional fabrication methods. The physical properties of the hydrogel and the print parameters affect the ability of materials to be printed into a structure that can faithfully match the designed model and characterizing the printability of materials has attracted considerable attention.

After fabrication, the developed hydrogel scaffolds when implanted in vivo experience physical impacts (e.g. compression) and chemical impacts (e.g. tissue regeneration and scaffold degradation). These impacts cause mechanical deformation of the hydrogel scaffold in the physiological environment that may result in a collapse of the scaffold and subsequently

compromise therapeutic functions. Therefore, it is vital to analyze the mechanical deformation under these conditions, and these techniques can be evaluated in an environment that mimics physiological conditions. This needs to be achieved by non-destructive methods of visualizing the hydrogel scaffolds in physiological conditions. However, this type of visualizing of the mechanical deformation of implanted hydrogel scaffolds has not been reported yet.

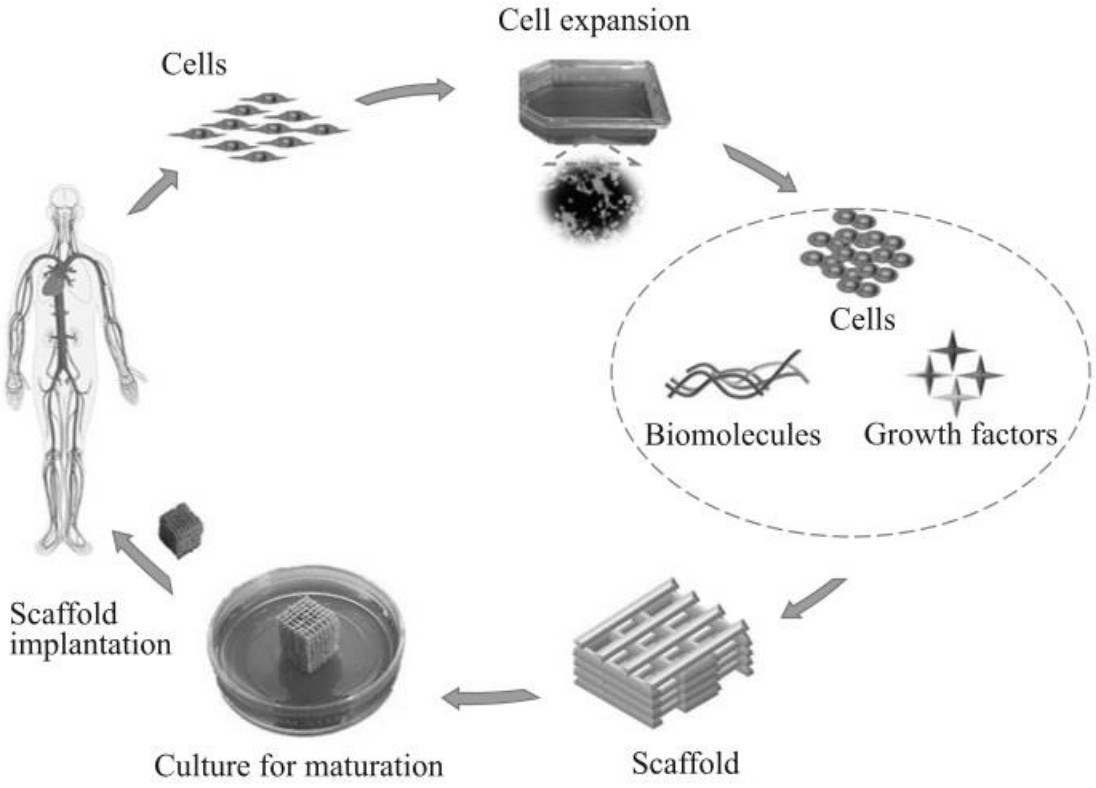

Figure 1.1Principle of tissue engineering [2]

The commonly available non-destructive imaging modalities in tissue engineering [9-12] are as follows: X-ray micro-computed tomography (μCT), ultrasound imaging (USI), and magnetic resonance imaging (MRI), however, these modalities are not ideal. The μCT, a conventional imaging technique, facilitates non-destructive imaging with 3D structures [13,14]. The conventional μCT is challenging to visualize low-density materials due to the low X-ray absorption attenuation. On the other hand, MRI cannot be used to image implanted hydrogels that have similar density like soft tissues, the difficulty in achieving high spatial resolution (limited to submillimeter level) and cannot achieve scanning the microstructures of hydrogel scaffold [15].

Imaging with ultrasound allows for non-destructive imaging of soft tissue, but its application in quantitative analysis is limited because of its low spatial resolution (100 µm to a few hundred microns) [16]. These modalities are not ideal for imaging of hydrogel scaffolds.

Alternatively, the synchrotron propagation-based imaging technique (SR-PBI) technique holds great promise for non-destructive imaging of hydrogel scaffolds due to the ability to use phase-contrast imaging techniques. The high resolution and high contrast images from SR-PBI are achieved by capturing refracted X-rays with high-resolution detectors. By combining SR-PBI with computed tomography (SR-PBI-CT), this technique allowed for capturing 3D microstructure information of hydrogel scaffolds. The combination of a synchrotron that offers high-energy and intense brilliant light from a point-light source and high-resolution X-ray detectors with computed tomography has demonstrated an unparalleled capability for visualizing and distinguishing soft tissues [17]. This study aims to explore SR-PBI-CT imaging parameters for practical hydrogel imaging and to take advantage of the technique to characterize printability and scaffold mechanical deformation.

1.2. Literature Review

1.2.1 Scaffold fabrication techniques and bioprinting

Many scaffolds for tissue engineering have been fabricated by using conventional techniques like electrospinning, solvent casting, freeze-drying, particulate-leaching, gas foaming, melt moulding, phase separation[18]. An emerging technique - 3D bioprinting is one based on additive manufacturing technology, for fabricating scaffolds or tissue constructs with arbitrary geometry to print successive layers of desired structure for tissue repair or regeneration [19]. Notably, the conventional technique possesses considerable limitations like precise control of pore size, patient-specific scaffold geometry, and increased amount of material utilization for fabrication than 3D printing. 3D printing allows excellent control of internal hydrogel structure, pore size, and external geometry in a precise manner comparatively better than conventional fabrication methods [20]. 3D printing permits the incorporation of biological factors such as living cells, growth factors, and drugs into the scaffolds during fabrication. Thus, it is possible to develop scaffolds mimicking the native tissues. It also influences 3D cell-matrix interactions, which is vital in the signalling pathway.

Bio fabrication technique through 3D bioprinting works by the principle of transforming digital images and digital objects obtained from CT/MRI and CAD software, respectively, into physical 3D structures [21]. 3D bioprinting is a subset of 3D printing that performs precise positing of biological materials with controlled spatial arrangement leads to multiple innovations in tissue engineering. The 3D printing technologies used for bioprinting biological materials are inkjet bioprinting, micro extrusion bioprinting, laser-assisted bioprinting, multi-photon excitation (MPE) based bioprinting [22,23]. Among the available methods, three major methods used in fabricating 3D hydrogel-based scaffolds are extrusion-based bioprinting, droplet-based bioprinting, and laser-assisted bioprinting [24]. Extrusion-based printing, employed in the present study can support the large-scale scaffold printing and printing of cells with high density, which is limited in other printing techniques [2].

1.2.2 Extrusion-based Bioprinting

Extrusion-based bioprinting (EBB) is a rapidly developing technology making substantial progress in tissue engineering and has full versatility in bioprinting biological tissue with cells [25]. Fabrication of implantable scaffolds for tissue regeneration and drug-delivering biodegradable tissue constructs for local drug delivery is feasible by extrusion bioprinting [26]. EBB enables bioprinting of cell-laden aggregates, cell hydrogels, bio-ink, micro-carriers, and decellularized matrix components. The foremost advantage in EBB is the ability to bioprint with high cell density, which is not possible with other bioprinting techniques [25]. EBB functions by extrusion of materials by robotic control onto the substrate by extrusion head [22], and this will be discussed in more detail below. Extrusion bioprinters generally consist of a dispensing head, printing stage, and control system for temperature and position (Figure 1.2). The categorization of the extrusion-based bioprinting system is three types based on dispensing or printing mechanism as follows: (i) pneumatic, (ii) piston-driven, and (iii) screw-driven.

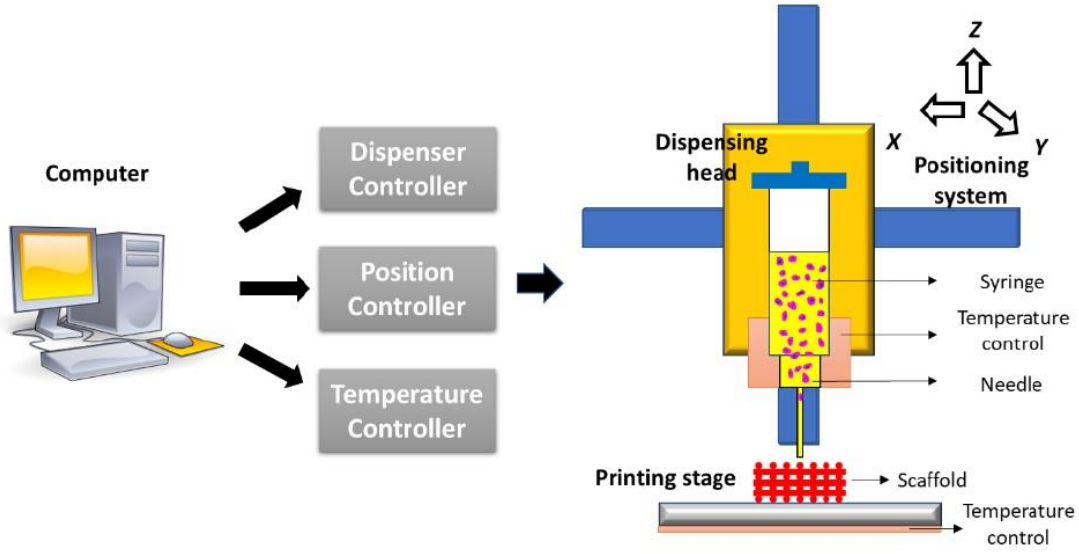

Figure 1.2 Schematic diagram of extrusion-based printing [2]

The extrusion-based printing works by the principle of fluid extrusion, dispensing the biomaterial ink continuously through the needle from the syringe under mechanical force (e.g. pressure) onto the printing stage [2]. The control in three axial planes (x, y, z-direction) of dispensing head consisting of needle and syringe, support printing of hydrogel scaffolds on the printing stage. The printing process is controlled by the three controllers: a) dispenser control, b) position control, and c) temperature control, having interfaced with the computer PC. The minimum resolution of the strands that can be achieved by this printing technique is in the order of 100 μm to 150 μm depending on the needle diameter [2,25,27]. The printed hydrogel scaffolds that require cross-linking and the cross-linking mechanism can be categorized as chemical cross-linking, photo-crosslinking, and physical cross-linking [23]. These cross-linking mechanisms can greatly facilitate the formation of networks to obtain 3D structures when printing.

The cross-linking of hydrogels takes time, and during that time, the printed hydrogel is in a solution form or semi-solution form and thus can deform on the printing stage. In this case, the printed structure differs from the designed one. Sometimes, the printed structure may collapse and suffer to form 3D structures. As a result, such biomaterial is considered as un-printable. Hence, the printability assessment is vital in printing hydrogel scaffolds.

Generally, hydrogel scaffolds are printed with different structural properties (e.g., geometry, size, and porosity) for targeted tissue regeneration [22,26]. The printability of the hydrogel is mainly affected by the number of printing parameters (e.g. printing speed, extrusion pressure, temperature, etc.) [12]. Regulating the printing parameters to obtain finer microstructures is vital in 3D fabrication. The primary motivation to characterize printability is that the designed structural properties may vary to a certain extent from the printed hydrogel structural properties. Therefore, characterizing the printability to create hydrogels with designed structures that can mimic the targeted tissues. It can be characterized by the measurement difference (e.g. strand size, pore size, etc.) between the printed hydrogel and the designed structure, which has attracted interest to improve the hydrogel and scaffold designs further. Currently, for the characterization of printability, the simplified printed structures (e.g. one or two printed layers of scaffolds) are utilized. As a result, the characterized results of the simplified structure may lack the ability to predict the printability of 3D hydrogel scaffolds after printing [28]. To analyze the printability of the hydrogel scaffolds, researchers need to understand the actual 3D structure of the scaffolds. Images of internal 3D structures of printed hydrogel scaffolds can be obtained with the aid of a synchrotron-based imaging technique [29].

1.2.3 Gelatin Methacrylate Scaffolds

The field of tissue engineering, through the use of scaffolds, has the potential to revolutionize the way of treatments for tissue repair and damage using hydrogel scaffolds. These scaffolds are often constructed from hydrogels, which are hydrophilic polymers having the capacity to hold a large amount of water content [30]. This is why the design and selection of the underlying polymers are important, as this dictates the physical and biological properties of hydrogel [31,32]. It is critical to control these properties in a hydrogel (e.g. a hydrogel that is mechanically strong but chemically inert [30]) and thus commonly compensated by the addition of another biomaterial. Hence, it is essential to note that the blending of these polymers is additive rather than transformational. So, a dynamic hydrogel GelMA having excellent biocompatibility and tunable mechanical properties have been reviewed and to characterize its printability and mechanical deformation [33].

Collagen has applications in various medical treatments. The presence of collagen in hydrogels could allow the cells to recognize the scaffold material and serve as a better scaffold platform for tissue engineering. However, due to the poor mechanical properties of collagen, it has limited applications in 3D fabrication. Gelatin is a denatured and degraded form of collagen and possesses similar biological and mechanical properties to native collagen. Gelatin can be 3D printed, but gelatin is quite challenging to print due to poor heat stability, high water solubility, and poor mechanical properties, and requires additional supporting biomaterials as a combination. Gelatin can be modified with methacrylic anhydride to create GelMA, which has similar biological properties to collagen and gelatin but with tunable mechanical properties. This makes GelMA suitable for various tissue engineering applications such as a 3D hydrogel scaffolds [34]. The applications of GelMA scaffolds are illustrated in Figure 1.3:

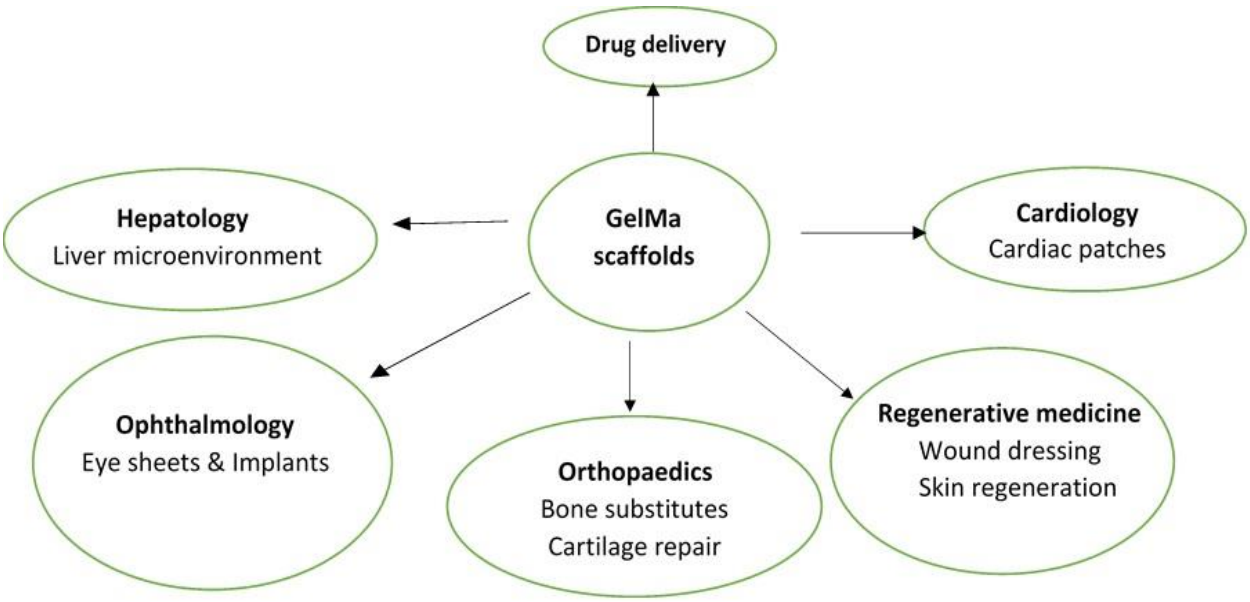

Figure 1.3 Biomedical applications of GelMA scaffolds [33,35–37]

1.2.4 Scaffold Visualization and Characterization

Imaging scaffolds in tissue engineering involves various range of destructive and non-destructive imaging techniques to analyze the structural, biological, and mechanical properties of 3D printed scaffolds. There is a great need for non-destructive imaging techniques to analyze the printability and mechanical properties, both for *in vitro* and *in vivo* research. The commonly

used imaging techniques available in tissue engineering to study the 3D structural status are discussed below.

The destructive imaging modality - scanning electron microscopy (SEM) is used as a standard visualization technique with a high-energy beam of electrons for structural analysis to produce exceptional topographical, crystallographic, and morphological features of the scaffolds [38]. The scanning electron microscopy produces high-resolution images ranging from 1 to 20 nm in size with a field depth of few millimetres to yield 3D appearances for better structural analysis [17]. Though the images of SEM provide details of pore size, strand diameter and estimates, the interconnectivity of fibres, cross-sectional area, or thickness of the strands [39]; this technique is not suitable for hydrogel scaffold visualization since the samples are required in the form of dry conditions to withstand a high vacuum [40], which entirely is a different environment to mimic the physiological condition.

Another destructive imaging modality - transmission electron microscopy (TEM) is also another electron microscope designed to observe at a cellular level with the spatial resolution of 1 nm and an imaging depth of about 100 nm. It is used to perform chemical analysis and can also reveal the details of the internal structure. TEM requires the samples to be sliced into a very fine thinner than 100nm for the effective transmission of electrons [39]. This technique does not apply to this current research since the study evaluates the full structure of the scaffold to evaluate the printability and deformation under compression. This technique also does not work with scaffolds inside living animals.

A conventional non-destructive imaging modality – μCT is a technique developed by computer processing with a spatial resolution up to a micrometre level ranging between 6 μm and 50 μm with the help of contrast agents. In recent years, the applications of μCT are enormous in research areas, including tissue engineering. μCT is a well-built non-destructive technique with high-resolution imaging and three-dimensional visualization with voxel size up to 1 μm, which is better compared to ultrasound imaging and magnetic resonance imaging [41]. Also, μCT has been considered as a gold standard for imaging bone explants', but it is not well equipped for soft tissue imaging as compared to dry state porous scaffolds. The high radiation dose for live animal imaging is a significant con with a micro-CT imaging technique [42]. The imaging setup is limited for

smaller size samples, where it is quite challenging for larger size samples. Also, the scan time is long for micro-CT and eventually increases the exposure time to samples if considered for live animal imaging. Though μCT facilitates non-destructive imaging with 3D structures, the critical challenge in conventional absorption-based μCT is to visualize low-density materials due to the low X-ray absorption attenuation. By considering the limitations above, it is evident that this technique is not effective for hydrogel scaffolds since hydrogels have similar densities and radiopacity as soft tissue, so it would be challenging to visualize the hydrogels with this technique without any contrast agents.

MRI is widely available in clinical researches *in vivo* allows for the gathering of pertinent information over the interest region in a detailed manner by a non-destructive method. For visualization, this technique uses magnetic fields and radio waves. MRI can best suit for long scan times as there is no radiation exposure to the samples. Though the imaging depth of this technique is high (whole organ), the spatial resolution (submillimeter level) is limited for its application in tissue engineering research, especially in hydrogel-based imaging [43]. Hence, this technique is not a suitable imaging method for the quantitative characterization of hydrogel-based scaffolds.

USI is also an established non-destructive imaging modality that provides structural tissue information by transduction and reflection of high-frequency sound waves. This modality works on electrically driven high-frequency (>20 kHz) oscillation of a piezoelectric crystal in the transducer probe. This technique possesses the advantage of relatively cheaper, safe, provide real-time information and non-destructive to samples. USI technique has applications in tissue engineering, such as visualization of microvascular networks. Though the spatial resolution is 100 μm to a few hundred microns, yet it is limited for quantitative analysis because of direct trade-off between imaging depth and spatial resolution [44]. Further, this imaging modality can be easily hindered by speckle noise and limited soft tissues, hydrogels contrast [10].

An alternative to the conventional non-destructive imaging techniques is a synchrotron-based imaging technique to visualize hydrogel scaffolds. In X-ray imaging, synchrotron radiation is a brilliant light source producing X-rays of high photon flux and coherence. Synchrotron-based X-ray imaging has a more significant potential for the development of new imaging methods in comparison with conventional X-ray imaging. The main synchrotron-based x-ray imaging

techniques are Absorption Contrast Imaging (ACI), Phase Contrast Imaging (PCI), and K-Edge Subtraction (KES) imaging. All the synchrotron-based X-ray imaging can combine with CT, such as absorption-CT, PCI-CT, KES-CT. Due to the combination of synchrotron-based techniques with CT, it delivers quantitative and isotropic 3D data. The most suitable and feasible synchrotron-based X-ray imaging technique considered for hydrogels visualization is propagation-based imaging (PBI or phase propagation imaging). [45].

X-ray phase-contrast imaging (PCI) are techniques, experimentally proven to image biological soft tissues without staining [46] with the help of refracted X-rays by the sample to form an image. The imaging techniques enhance the edges and produce fine details of the internal boundaries of a sample. The techniques are good at visualizing the low-density materials, which are challenging to image using conventional X-ray radiograph. The primary objective of X-ray phase-contrast imaging is to determine 2D or 3D radiographs of an object by phase changes of the transmitted X-ray radiation and by recording attenuation. In general, X-rays PCI techniques are inevitable techniques in medical diagnostics, material science [47], and also making a benchmark in tissue engineering. It is because of using various in shifts of X-ray radiation which passes through scaffolds, and other soft tissues with different refractive indexes, electron densities, and atomic numbers while scanning without any exogenous contrast reagents [48]. The five major classifications of phase-contrast imaging are propagation-based imaging (PBI), analyzer-based imaging (ABI), Crystal interferometry, grating interferometry, and grating non-interferometry [49]. Since the addition of phase contrast is essential in imaging hydrogel scaffolds, the PBI is employed in this research, and its importance is stated below.

The setup of propagation-based imaging consists of the detector being placed away from the sample at a distance ranging from few millimetres to centimetres (near field imaging (NFI) to phase propagation imaging (PPI) as shown in figure. 1.4) [49]. This setup facilitates prominent refraction (bending) of X-rays resulting in sharper contrast at edges. This imaging technique allows for the enhancement of the edges of tissue-engineered scaffolds in the radiographs and produces fine details of the internal boundaries of a sample. The visualization of low-density materials becomes possible using SR-PBI compared to conventional X-ray imaging. Combining SR-PBI with computed tomography (SR-PBI-CT), this technique allows us to obtain 3D microstructure

information of hydrogel scaffolds. This is why this method is becoming an ideal solution for visualizing the structure of the low-density materials.

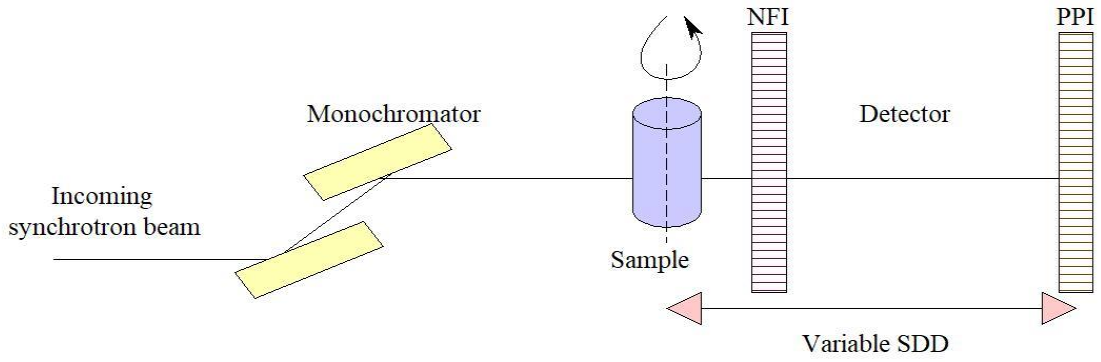

Figure 1.4 The schematic experimental setup of synchrotron propagation-based imaging with computed tomography.

1.2.5 Research Issues

In the field of tissue engineering, various visualization techniques are available to study and characterize the biological, mechanical, and morphological properties of the tissue-engineered scaffolds. At present, the available techniques to assess printability limit the number of layers and generally demand specific treatment to perform the imaging. For example, commonly available imaging techniques like SEM and TEM require a high vacuum environment for imaging and thin sectioning of samples during sample preparation, respectively. These imaging techniques are destructive, and they may change or even damage the scaffold structure. The results obtained from scaffolds with the simplified structures or with a limited number of layers might not accurately represent the printability results for 3D scaffolds having more layers of complex structures [50].

μCT facilitates non-destructive imaging with 3D data for quantification without contrast staining. But, the critical challenge in conventional absorption-based micro-computed tomography is imaging similar low-density materials (hydrogel and tissues) due to low x-ray attenuation. Hence, micro-computed tomography provides reduced sensitivity to similar low-densities materials [39,51]. Also, imaging techniques like MRI and USI can provide low spatial resolution in hydrogel scaffold visualization [11,44]. Therefore, the limited capability of non-destructive

imaging techniques to visualize the hydrogel structural status *in vitro* and *in vivo* conditions has been a significant research gap.

The printed hydrogel scaffolds, when implanted *in vivo*, experience physical impacts (e.g. compression) and chemical impacts (e.g. tissue regeneration and scaffold degradation). These impacts cause the deformation of the hydrogel scaffold in a physiological environment. Hence, the deformation of the scaffold, both *in vitro* and *in vivo*, is essential to understand the strength and behaviour of the printed hydrogels and to help to design a robust structure that will maintain their functions *in vivo* until it gets replaced by regenerative tissues. However, it appears that the evaluation of the success status of scaffolds under these conditions has not been done earlier, as there is no literature available to the best of our knowledge.

1.3. Research Objectives

The goal of this research is to develop the novel imaging method based on the synchrotron imaging technique, and to characterize the printability and deformation of printed hydrogel scaffolds using this method. The following specific objectives or major tasks were pursued to achieve this goal.

1. Study SR-PBI-CT imaging to non-destructively visualize the printed hydrogel scaffolds in wet condition.

2. 3D print the GelMA hydrogel scaffolds, and non-destructively characterize the printability of the scaffolds fabricated with different printing speeds and compressions under different deformation levels using SR-PBI-CT.

1.4. Organization of Thesis

This thesis consists of five chapters, including this chapter. Each of the other chapters are briefly summarized as follows.

The first chapter includes the background to the present work, a literature review of 3D fabrication technique using extrusion-based printing, the biomedical importance of hydrogel (GelMA) used in this research, and the currently most available imaging techniques in tissue

engineering research, and the research gap found from the literature review, objectives to fulfill the research gap and the thesis outline.

The second chapter describes the methods of synthesis and preparation of GelMA ink, printing and photocuring of GelMA scaffolds, and the characterization of printed GelMA scaffolds in terms of printability and mechanical deformation under compression with the evaluation criteria involved in assessing the printability and deformation were mentioned with equations.

The third chapter explains the methods of imaging setup for SR-PBI-CT conducted at the Canadian Light Source (CLS). The examination of image quality was used to determine the appropriate sample to detector distance (SDD), energy, and the number of projections in CT scans.

The fourth chapter of this thesis presents and discusses the results: (1) the examination of SR-PBI-CT system for hydrogel imaging and the influence of SDD, energy, and the number of projections on the image quality, (2) the effect of printing speed on hydrogel scaffold printability and (3) the evaluation of structural status under normal compression levels. Each section is evaluated by the parameters mentioned in the second chapter.

The last chapter presents the conclusion drawn from the research, along with the discussion on the research limitation and contribution as well as on the potential future work suggestions.

CHAPTER 2. MATERIALS AND METHODS FOR GELMA SCAFFOLDS

2.1 Synthesis of GelMA biomaterial

The GelMA biomaterial was produced by the reaction of gelatin from porcine skin (Sigma Aldrich – G2500) in the presence of methacrylic anhydride (Sigma Aldrich – 276685). During the synthesis of GelMA, the amino groups in the gelatin are replaced by methacryloyl groups in methacrylic anhydride, resulting in modified gelatin. When the photo-initiator is added to the modified gelatin solution, in the presence of UV light due to the existence of methacryloyl groups, photo cross-linked GelMA hydrogels are produced [52].

The detailed protocol involved in the synthesis of GelMA biomaterial and printing ink (5% concentration) is stated below [53] (Figure):

1. Dissolve 30 g of gelatin type A from porcine skin with gel strength 300 (Sigma Aldrich) in 300 mL of Dulbecco's phosphate-buffered saline (DPBS) at 60 ºC for 3 hours.

2. Allow the temperature of the solution to cool to 50 ºC to add methacrylic anhydride under the fume hood.

3. Add 24 mL of methacrylic anhydride at a rate of 1mL/min drop by drop at 50 ºC which took 24 minutes for complete addition.

4. Allow the solution to react for 3 hours at 50 ºC under dark condition.

5. Add 324 mL of warmed DPBS at 40 ºC to stop the methacrylate reaction.

6. Dialysis the solution with distilled water at 40 ºC for 15 days to thoroughly remove the methacrylic anhydride solution.

7. Freeze dry and store the dialyzed solution at -40 ºC for five days.

8. After five days, the materials should be stored in -40 ºC freezer.

9. To prepare printing ink, dissolve 0.5% (w/v) of 2-Hydroxy-4′-(2-hydroxyethoxy)-2-methylpropiophenone (Sigma Aldrich – 410896) (photo-initiator) to the desired volume of Phosphate Buffered Solution (PBS) containing 5% GelMA at 80 ºC for 4 hours.

10. Add 0.1% of Polyethylene glycol (PEG) to the GelMA/PBS solution to further improve the mechanical properties (e.g. mechanical strength) of GelMA.

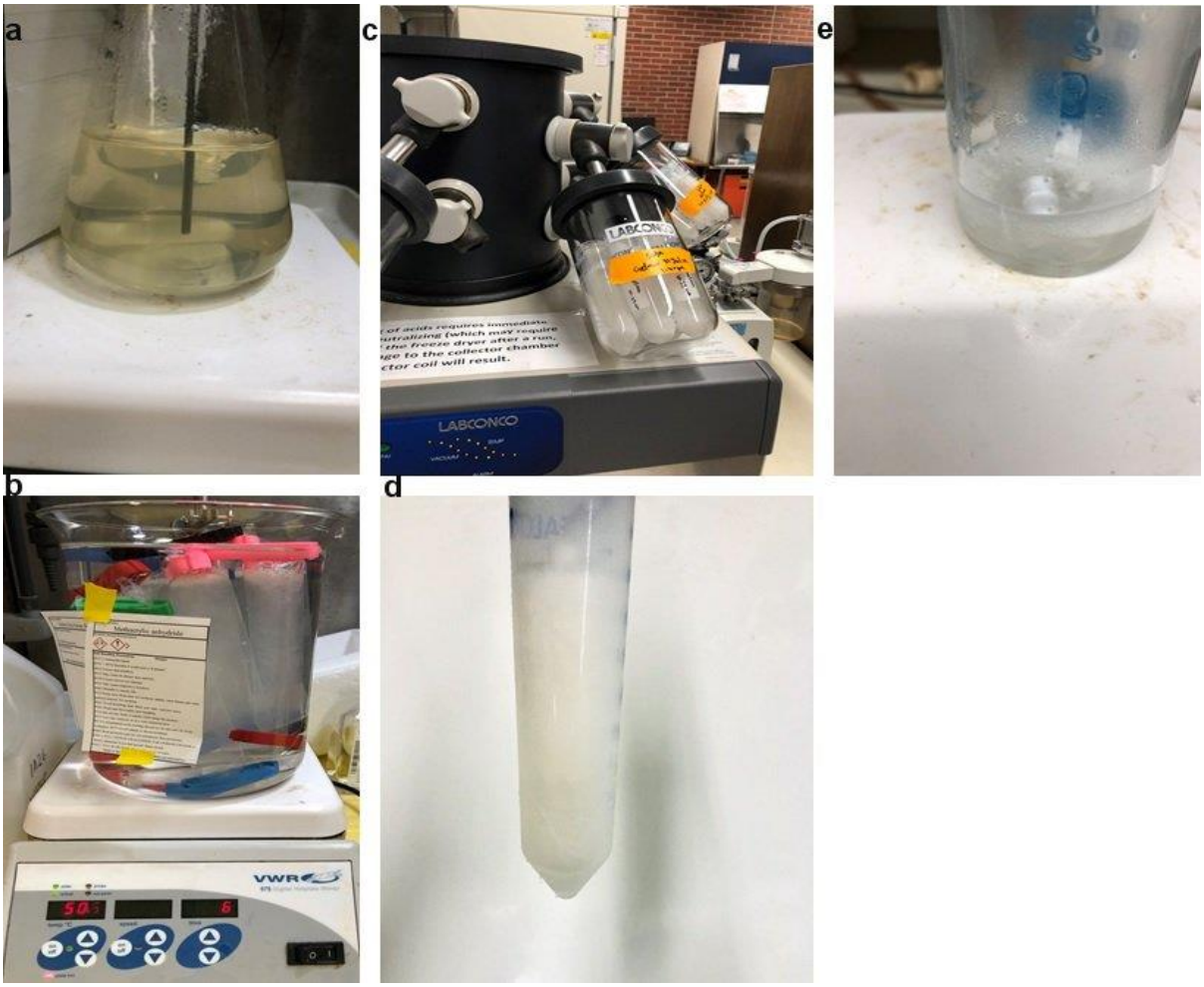

Figure 2.1 Procedures to prepare GelMA biomaterial and printing ink at Biofabrication laboratory; (a) Addition of Gelatin to PBS ; (b) Dialysis of the synthesized solution after addition of Methacrylic anhydride ; (c) Freeze-drying of dialyzed solution at – 40 ºC for five days ; (d) Freeze-dried GelMA biomaterials to store at – 40 ºC freezer; and (e) Addition of photo-initiator and PEG to PBS solution containing GelMA to prepare printing ink.

2.2 3D printing of scaffolds

Magic13 Envisiontec software was used to design a digital model of the scaffold to be printed. The designed 3D model was loaded to the VisualMachine software, which is interfaced with the 3D printer. Extrusion based 3D printing technique has been employed to print 3D scaffolds using a 3D bioplotter (Envision TEC Inc., German) (Figure 2.2). The hydrogel scaffold utilized for all experiments (alginate scaffold for the SR-PBI-CT examination and GelMA scaffolds for printability and mechanical deformation characterization) were fabricated with a dimension of 10 x 10 x 5 mm, and the designed diameter of each strand was 200 µm.

For the fabrication of alginate hydrogels, the preferred printing pressure was 0.2 bar pressure, and the printing temperature was 27 ºC. The alginate scaffolds were printed with the printing speed between 12 mm/s and 14 mm/s. During the printing of the alginate scaffold, Calcium chloride (CaCl2) served as a cross-linker of alginate hydrogel was placed on the scaffold holding stage. In this study, 50uM of CaCl2 was used while printing and 100uM of CaCl2 was used after printing to preserve the fabricated hydrogels at 4 ºC.

For the fabrication of GelMA hydrogels, the preferred printing pressure was 0.1 bar pressure, and the printing temperature was 25 ºC. The GelMA scaffolds were fabricated with different printing speeds of between 14 mm/s, 16 mm/s, and 18 mm/s to characterize printability. The hydrogels were printed in an open-air environment without any supporting bath. Hence, during printing, the scaffold holding stage (Figure 2.2) was kept at 0 ºC to withhold the hydrogel structure. After printing, the fabricated hydrogels were immediately cross-linked with ultra-violet (UV) light rays.

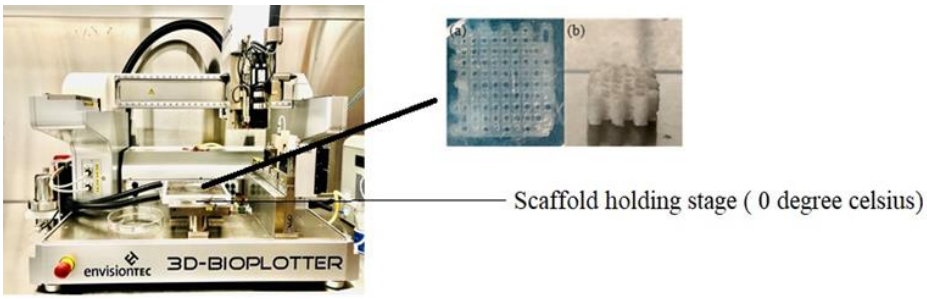

Figure 2.2 3D printer to fabricate 3D hydrogels; Images of 3D printed hydrogel scaffold: (a) top view; and (b) side view.

2.2.1 Photo curing of GelMA scaffolds

The long-wave UV light lamp (RAD-FREE from Schleicher & Schuell) having the UV light wavelength of 365 nm was utilized to cross-link the printed 3D scaffolds after fabrication. The printed scaffolds were cross-linked for 240 seconds by keeping at a distance of 110 mm away from the UV light lamp (Figure). For immediate cross-linking, the UV light lamp setup was made near the 3D printer, as shown in figure 2.3. to obtain 3D cross-linked hydrogels.

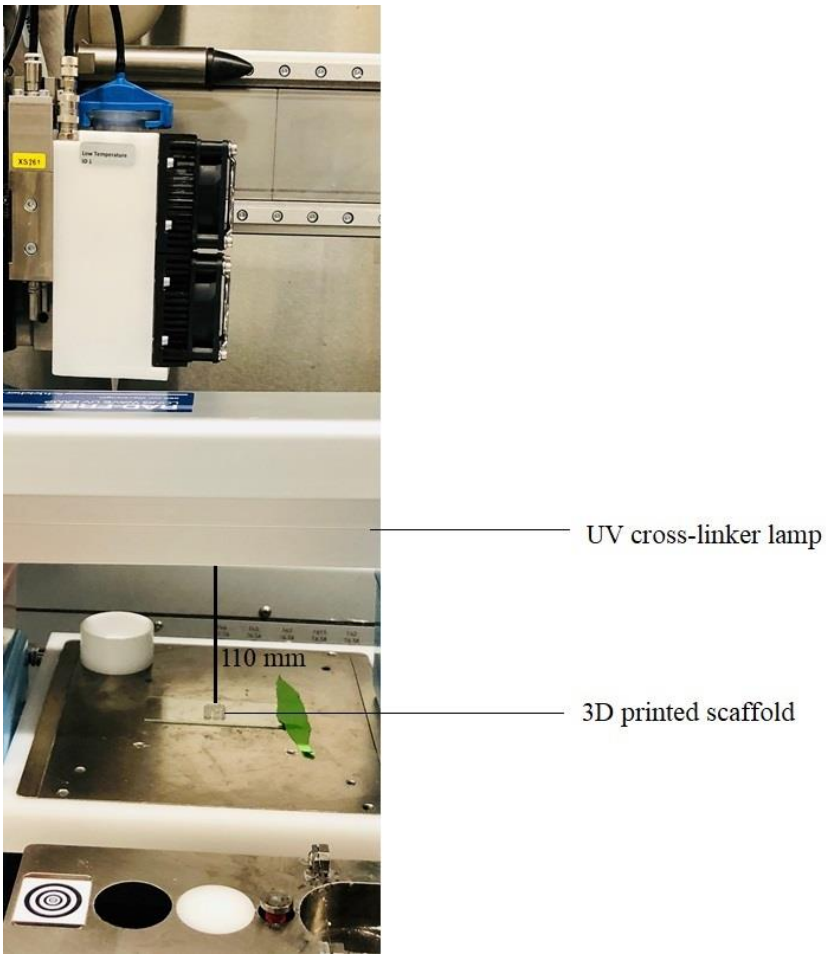

Figure 2.3 Cross-linking UV lamp setup for 3D printed GelMA scaffold having a distance of 10 mm away from the cross-linker source.

2.3 Characterization of GelMA scaffolds

2.3.1 Printability assessment

The GelMA hydrogels fabricated with 0˚ - 90˚ strand orientation was utilized for the characterization of printability and deformation behaviour. The parameters selected for the characterization were strand diameter (side view along the z-direction) and pore size in the z-axis or x-y axis (top view in x-y axis). The strand diameter and pore size of the hydrogels were calculated from the randomly selected images (N=3) from different layers of the scaffolds. The average strand diameter and pore size (n=9; 3 calculations were made from each image) was measured to assess the strand diameter printability factor Ds (equation 2.2) is calculated by measuring the printed strand diameter divided by the designed diameter of the strand and pore size factor Pxy is measured by the printed pore size divided by the designed pore size, with the resulted Pxy, to characterize scaffold pores in the x-y plane (equation 2.1) respectively [54]. The analyzed values close to 1 indicates best suitable printing speed.

$$P_{xy} = \frac{\text{measured pore size}}{\text{designed pore size}} \tag{2.1}$$

The D_s value and P_{xy} value close to 1 indicates the printing fidelity of the printing speed for GelMA scaffolds.

$$D_S = \frac{\text{diameter of printed strand}}{\text{designed strand diameter}} \tag{2.2}$$

For printability characterization, at least five GelMA scaffolds were printed at each printing speeds such as 14 mm/s, 16 mm/s, and 18 mm/s. At least two scaffolds at each printing speed were utilized for imaging. The best imaging result obtained at each printing speed was discussed in results chapter. So, the printability characterization results discussed the results of three best scaffold (one at each printing speed).

2.3.2 Estimation of GelMA scaffold deformation under compression

The characterization of deformation was carried out by analyzing the change in strand diameter and pore size in the x-y axis or along the z-axis. At each deformation level, the strand diameter and pore size of the hydrogels were calculated from the randomly selected images (N=3)

from different layers of the scaffolds. The average strand diameter and pore size (n=9; 3 calculations were made from each image) were calculated for all compression levels and normalized by the value of 0% compression. The normalized values of strand diameter and pore size smaller than 0.5 are considered as the pore disappeared, and strands fusion occurred, indicating a relatively weak structural status of the scaffolds under compressions.

For mechanical deformation characterization, at least five GelMA scaffolds were printed at 18 mm/s. At least three scaffolds were utilized for imaging. The best imaging result obtained was discussed in results chapter. So, the mechanical deformation characterization results discussed the results of the one best scaffold.

2.4 Statistical analysis

The printability experimental data were calculated and mentioned using mean and standard deviation values. Statistical significance was calculated by one-way analysis of variance method and found the data are unique with an acceptable significance level of $p<0.05$.

CHAPTER 3. SYNCHROTRON-BASED IMAGING SETUP AND IMAGE PROCESSING METHOD FOR SCAFFOLD VISUALIZATION

3.1 Synchrotron Propagation Based Imaging (SR-PBI) system setup

The SR-PBI-CT scans were carried out at the Bio-Medical Imaging and Therapy (BMIT) 05ID-2 beamline at the Canadian Light Source Inc. (Figure). The samples were imaged at 30 keV, 40 keV, 50 keV, and 60 keV for scanning parameters examination and at 30 keV for printability and also deformation experiments, while the SDD was set at 20 cm, 55 cm, 100 cm, 150 cm, and 200 cm for examination and for other experiments the scanning was done at 150cm. When the SDD was set at a minimum distance (20 cm), the scanning system was considered as a conventional absorption-based imaging setup; when the SDD was set at the distance of 150 cm, it was set for SR-PBI. The detector consists of an AA60 beam monitor coupled with ORCA Flash 4.0 (Hamamatsu Photonics, Shizuoka, Japan) with an adequate pixel size of 13.5 × 13.5 μm^2. During scanning, a specially treated container (*in-vitro* device) (Figure) with a diameter of 2.3 cm was loaded with a scaffold sample. This device was containing water as a surrounding environment has mounted on the sample stage. For the deformation study, before the scan, the modified syringe piston was pushed to provide compressive forces on scaffolds by controlling the position of the piston. This is performed with the aid of a measurement scale attached to the sample holder with 0.5 mm in resolution to keep track of the movement of the piston and compression level quantitatively. For high-resolution tomography, 1800 angular projections were acquired over 180° of sample rotation. The acquisition time per scan was approximately 5 minutes with on-the-fly mode, with the exposure time of ~60 milliseconds per projection. Flat-field and dark-field images were captured before each scan for background correction. UFO-KIT software was used for background correction, ring artifact removal, and CT reconstruction [55]. The projections were pre-processed with the phase retrieval algorithm Paganin/TIE [56]. ImageJ (1.52) and Avizo 9.7 (Thermofisher Scientific) were used for further image processing and 3D visualization.

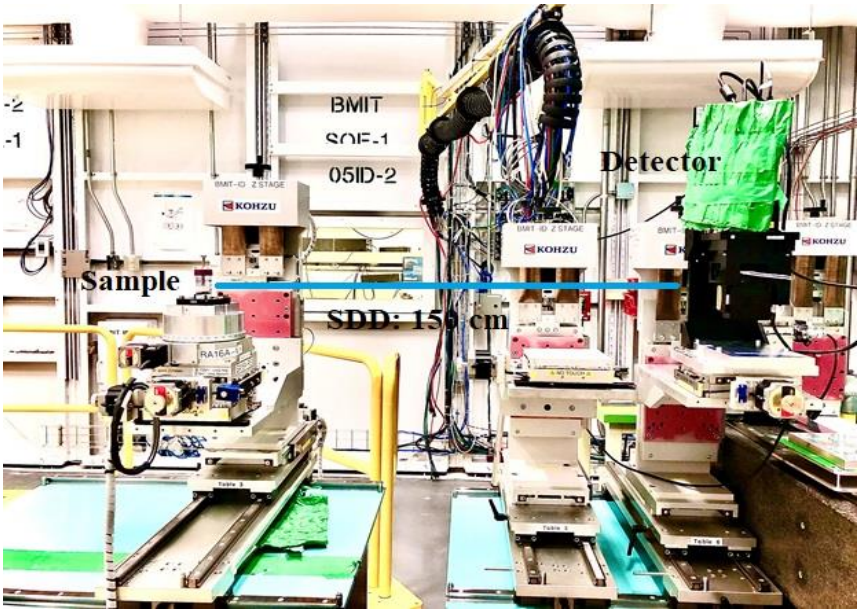

Figure 3.1 Synchrotron-based Propagation Based Imaging setup at the 05ID-2 beamline

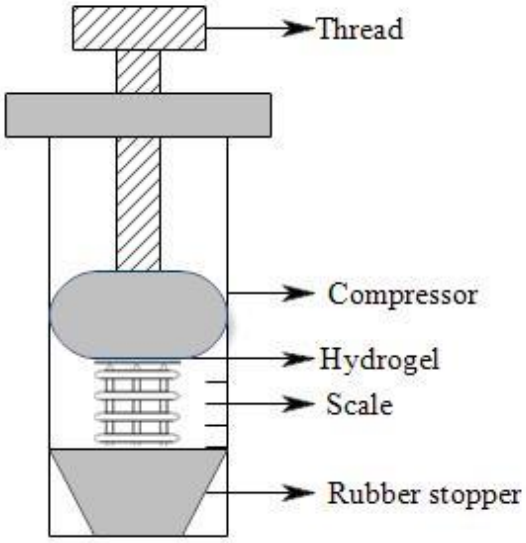

Figure 3.2 Schematic diagram of the in-vitro compression test device for hydrogel scaffolds

3.2 Image data analysis

The image quality assessment framed in this experiment is to exhibit the optimal scanning parameters to visualize hydrogel scaffolds. The quality of an image was evaluated based on the parameter Contrast-to-noise ratio (CNR). The spatial resolution in terms of the number of pixels

in the contrast-enhanced edge areas, and image intensity profiles were also calculated at some points to further emphasize the optimal findings.

The CNR was calculated as the contrast of an interest region in the image (hydrogel scaffold strand) to the noise of the background [57-59] based on the equation (3.1) [60].

$$\text{CNR} = \frac{\delta s}{\delta b} \tag{3.1}$$

where δs is the standard deviation of the interest region and δ_b is the standard deviation of a background noise region.

The value of δs was calculated on a square-shape area selected, which contains the hydrogel scaffold on the reconstructed images. The value of δ_b was on an area excluding hydrogel scaffolds of the same size in the images. The image resolution was measured from the profile image as the number of pixels in edge enhanced area (differentiating the hydrogel contour from the surrounding background medium). The profile images were obtained by drawing a line across the structured region to detect hydrogel signals.

For the SR-PBI-CT imaging examination, at least five alginate scaffolds were printed. At least three scaffolds were utilized for imaging. At least three scaffolds were imaged for different SDDs and different X-ray energies. The best imaging result obtained was discussed in the results chapter. So, the examination results of the SR-PBI-CT technique discussed the imaging results of one best scaffold for both different SDDs and X-ray energies. The same sample was imaged with different SDDs, so the imaging results are comparable.

CHAPTER 4. RESULTS AND DISCUSSION

4.1 Synchrotron Based Imaging for Hydrogel Scaffolds

The 3D visualization of the hydrogels is significant in tissue engineering research since the visualization with poor contrast and resolution can comprise in differentiating the tissue-engineered scaffolds and soft tissue or the physiological environment, accounting for challenges to pursue quantitative analyses. SR-PBI-CT imaging technique provides a non-destructive visualization of scaffolds with lower densities and weak X-ray absorption capacity [61,62]. Certain experimental factors can compromise the visualization or quality of images to a greater extent. The variation in the SDD, different X-ray energies and number of projections, possibly affect the quality of an image having fine details. Hence, to fine-tune the image quality, the examination of PBI parameters is essential for the quantitative analyses.

4.1.1 Effect of SDD on PBI images

The scaffolds can be visualized at the acceptable SDDs of 100 cm, 150 cm, and 200 cm shown in the Figure. 4.1 c-e. But the scaffolds at 20 cm and 55 cm (Figure a-b) are almost invisible, counting as unacceptable SDD for hydrogel imaging. Increasing the SDD, the contrast-to-noise ratio of the images improves, and the best image contrast happens in the longest SDD of 200 cm is evident in the figure. 4.1e & 4.2b. But, the long SDD, decreases spatial resolution by increasing pixels in the contrast-enhanced edge areas (figure 4.1 & 4.2a) indicates smaller the number of pixels, higher the spatial resolution. So, the lowest-resolution image is obtained at the longest SDD of 200 cm in this experiment (figure. 4.1e). To capture images with good contrast and resolution for hydrogel visualization, the acceptable SDD is figured out to perform hydrogel scanning. Based on the graphical analysis (figure 4.2b), 150 cm could be the acceptable SDD, since the CNR is comparatively higher than 100 cm and 55 cm, and no significant improvement of CNR was displayed at 200 cm. For the image resolution, the SDD of 150 cm could still be acceptable because the visualization of the hydrogel scaffold is challenging at 55 cm due to poor contrast (figure. 4.1b) though the resolution is higher than 100 cm, 150 cm, and 200 cm. Also, 100 cm could be bypassed as the PBI contrast is lesser than 150 cm. Therefore, the images obtained at the SDD of 150 cm

(figure. 4.1d) is further supported with good contrast and acceptable resolution, which is better than the image at the SDD of 200 cm (figure. 4.1e).

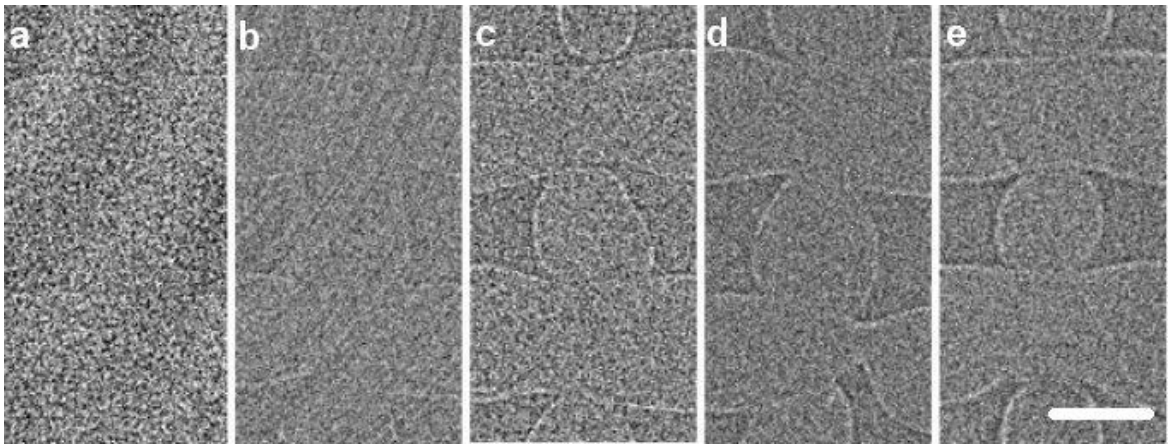

Figure 4.1 Comparison of reconstructed images with different SDDs of (a) 20 cm; (b) 55 cm; (c) 100 cm; (d) 150 cm; and (e) 200 cm. Scale bar indicates 1 mm

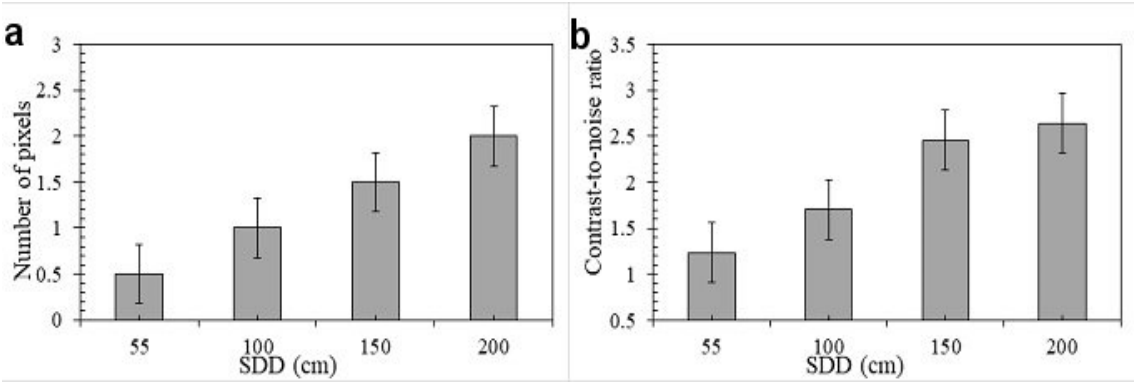

Figure 4.2 Comparison of (a) spatial resolution measured with the number of pixels at contrast-enhanced edge areas; and (b) CNR at different SDDs

The importance of contrast in visualizing the hydrogel scaffolds and the difference between the absorption contrast and phase contrast is explained by comparing the figure. 4.1a & 4.1d. For the absorption imaging method, the sample was placed very near to detector at 20 cm (figure. 4.1a), which is the near-field regime [63]. Absorption imaging capture the absorption attenuation differences in the transmission of X-rays as they pass through the hydrogel. However, hydrogels and surrounding component, which was water medium in this study, are having similar density resulting in poor absorption contrast of the hydrogel in the images. Whereas, propagation-based

imaging measures the refracted X-rays introducing phase shifts by the hydrogel with different refractive index [64,65]. With this property, it added an additional phase contrast to the hydrogel and enhanced the edge/border of the hydrogel scaffolds. To capture phase shifts of refracted X-rays through the hydrogel, the hydrogel was placed away from the detector with the SDD of 150 cm. It is seen from (Figure. 4.1a) that the hydrogel scaffold is almost invisible in the absorption-based image (SDD: 20 cm), while the structures of the hydrogel strands can be clearly seen in the edge-enhanced PBI image (Figure. 4.1d). The phase information plays a significant role in imaging the hydrogel when the X-ray absorption attenuation of the hydrogel is similar to that of the physiological environment.

The effective utilization of X-ray phase shifts information in PBI has effectively increased the image contrast. The results of CT image assessment confirmed the influence of imaging techniques such as propagation-based imaging and absorption-based imaging. Figure. 4.1a & 4.1d shows that the hydrogel scaffold strands are clearly visible in PBI images compared to those in absorption-based images. PBI images include both absorption contrast and phase contrast. In this case, since the absorption contrast of the hydrogel is poor, the phase contrast makes the main contribution to the visualization of the hydrogel scaffolds. So, the PBI technique shows great impacts in the studies of tissue-engineered hydrogel scaffolds.

Alginate hydrogel scaffolds were used in this imaging study and have been successfully visualized by SR-PBI-CT. Since the PBI image contrast are related to material density, the PBI also has high potentials in the studies of other hydrogel materials. In this study, the water medium was used to mimic the *in vivo* physiological environments, such as soft tissues, since they have a similar density. It is excellent and promising that the PBI could be used for non-destructive scaffold studies *in vivo*.

4.1.2 Effect of X-ray Energy on PBI images

The variation of the X-ray energy causes differences in image contrast. It is evident from (Figure. 4.3a-d) that the profile of the scaffolds is clearer in lower energy 30 keV than those at the higher energy levels. As the X-ray photon energy increases from 30keV to 60keV, the CNR of the images is significantly reduced (Figure. 4.4), demonstrating the increase in X-ray photon energy, lower the CNR. The decrease in the CNR is due to the decrease of the X-rays attenuation coefficient of

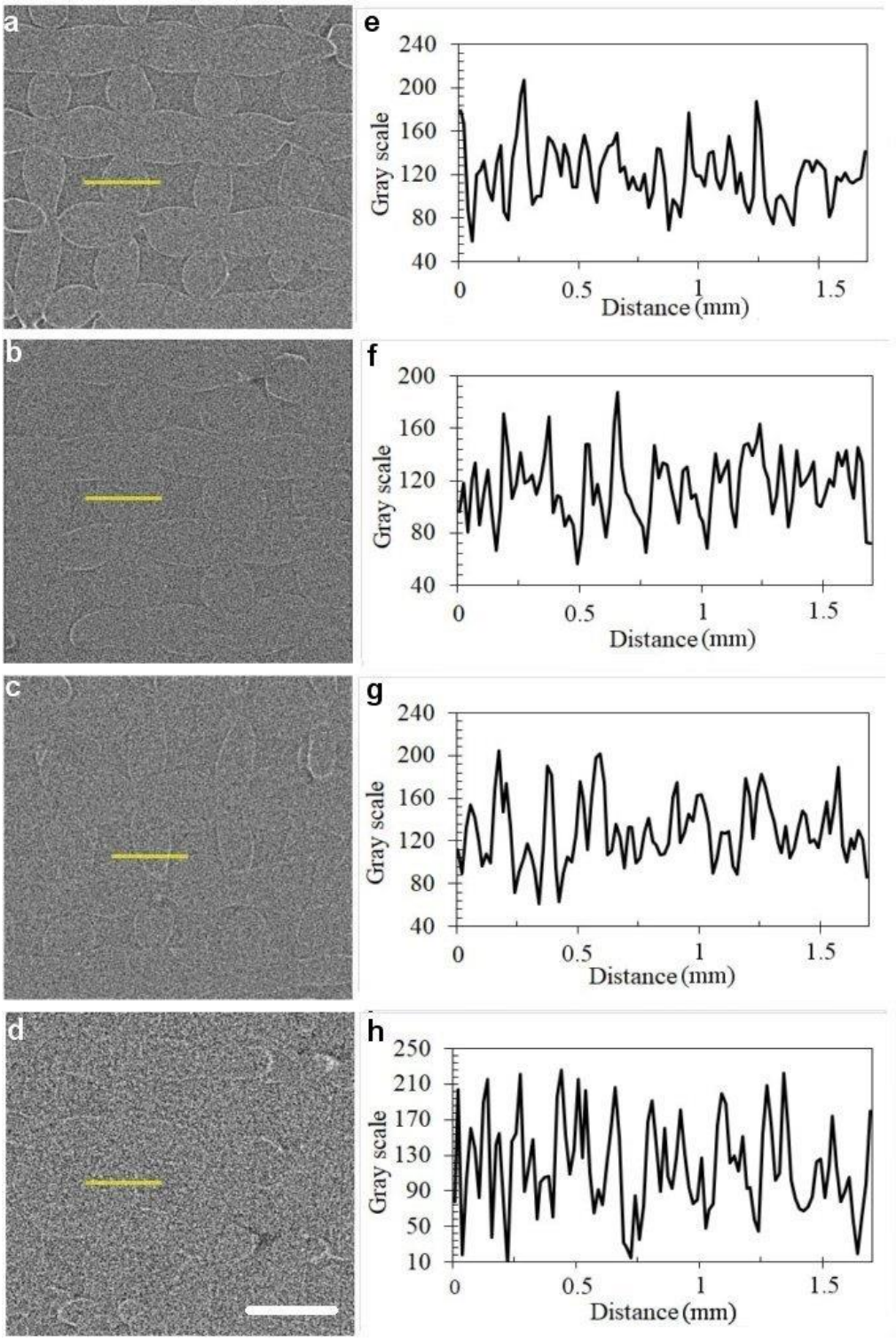

Figure 4.3 Comparison of reconstructed images at different X-ray energies of (a) 30 keV (b) 40 keV (c) 50 keV and (d) 60 keV. Intensity profiles (e), (f), (g), (h) of the yellow line drawn in figure (a), (b), (c), and (d). Scale bar indicates 1 mm.

the hydrogel with an increase in X-ray energy from 30 keV to 60 keV (36 % to 55 %). These results display that; lower X-ray energy produces an image with higher CNR. The lower energy limitation of the 05ID-2 beamline at CLS refrained from applying X-ray energy below 30 keV. Therefore, to obtain the image with good contrast, lower energy of 30keV would be recommended for hydrogel imaging with enough photon transmission.

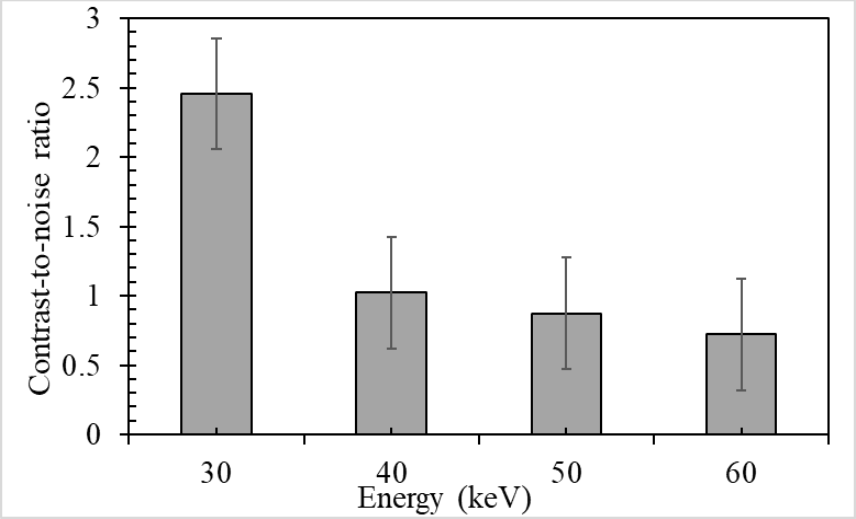

Figure 4.4 Comparison of the CNR of different reconstruction images at different X-ray energies

4.1.3 Image processing using Paganin-Transport of Intensity Equation (TIE) phase retrieval algorithm

For the improvement of image quality of the PBI-CT data to perform quantitative analysis, the Paganin/TIE algorithm was used for phase information retrieval during pre-image processing for the images obtained at SDD of 150 cm and 30keV energy. Compared with the non-phase retrieval reconstructed image (Figure 4.5a) (also called edge enhanced image), the phase retrieval reconstructed image (Figure. 4.5b) shows a much better image quality of the hydrogel scaffolds. The image contrast of phase retrieved images shown in the measured image profile (Figure. 4.5d) is significantly better than the image contrast of the non phase retrieved image (Figure. 4.5c). Also, the background noises in Figure 4.5b are much lower than figure. 4.5a. The phase retrieval converts the edge-enhanced contrast to areal contrast, and it also improves image contrast. The resultant image can be easily used for image segmentation and further quantification. The image quality

analysis from the figure. 4.5 depicts the importance of the Paganin-TIE algorithm in pre-image processing.

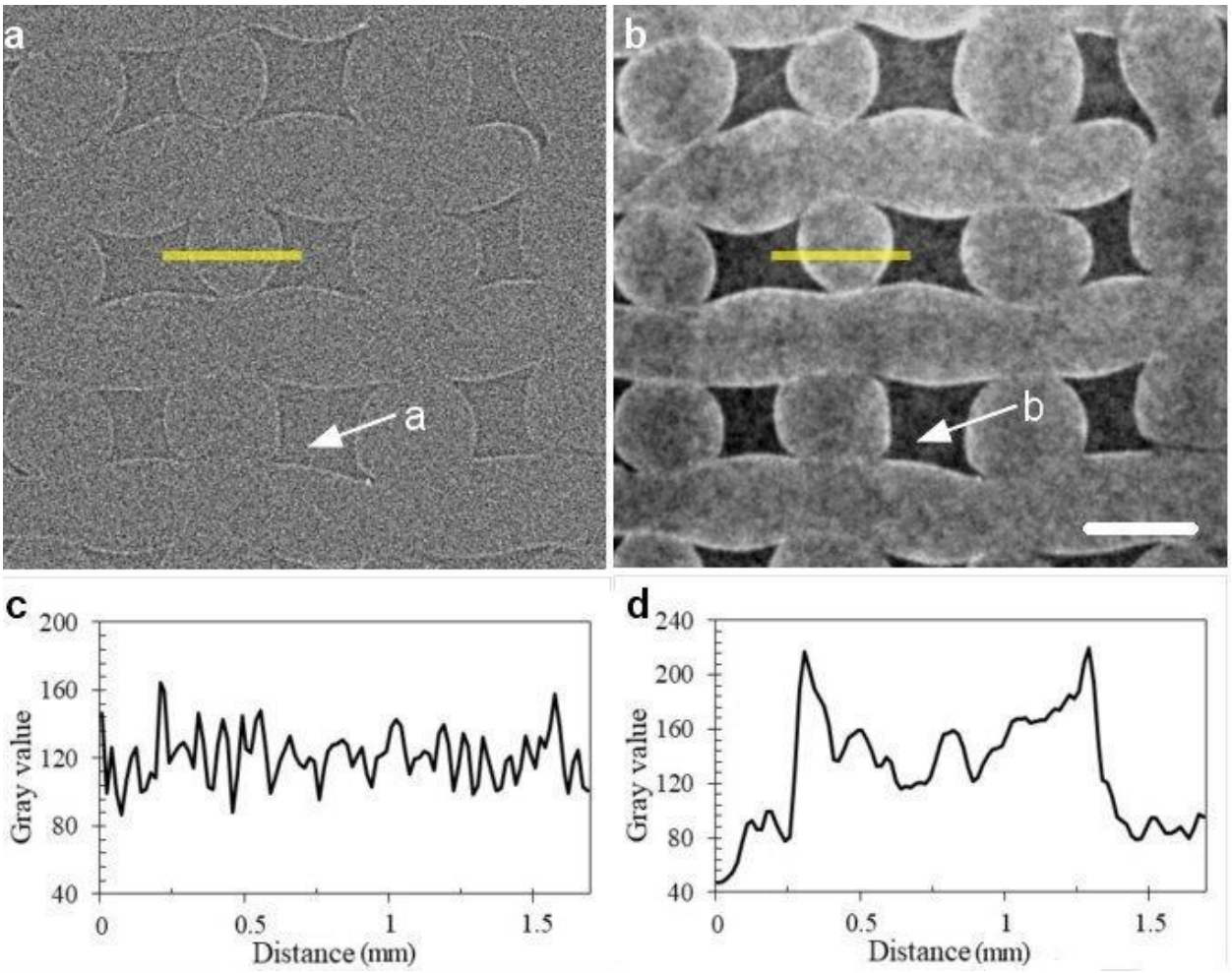

Figure 4.5 Comparison of non-phase retrieval and phase retrieval reconstruction images. (a) Non-phase retrieved the reconstructed image, and (b) phase retrieved reconstructed image (c) and (d) are the image profiles measured at the yellow line positions in (a) and (b), respectively. The arrows 'a' and 'b' in (a), (b) point to the background noise area. Scale bar indicates 1 mm.

Also, the quality of the images is further evaluated by the calculated CNR values, which serve as a useful characterizing tool to measure the noise level in an image quantitatively. The higher the value of CNR, the better the image quality and less noise. The CNR values were calculated for the non-phase retrieval PBI image and the phase retrieval PBI image. The CNR value of the phase retrieval image is 2.4, and the value of CNR is 1.6 for the non-phase retrieval image. The CNR

result repeatedly proves the significance of the phase retrieval image processing in the non-destructive visualization of the hydrogel scaffolds. This discussion confirms that the Paganin-TIE algorithm is vital in contrast enhancement with the ultimate purpose of analyzing hydrogel scaffolds.

4.1.4 3D rendering and quantification using phase retrieved reconstructed images

The phase retrieved images provide finer details of areal structures with better image contrast. After pre-processing, the phase retrieved images are suitable for segmenting hydrogel scaffolds out of the surrounding medium for quantitative analysis. The 3D reconstruction of phase retrieved images is performed by using Avizo 9.1 (FEI Company). By implementing segmentation based on the images, a 3D volume rendering model of the hydrogel scaffold can be built and figure. 4.6a shows part of the 3D scaffold model. Afterimage segmentation, the hydrogel material and pores can be separated for quantitative analysis. For example, the porosity of the hydrogel scaffold is measured at 22%. Also, the quantitative analysis based on the reconstructed images has been performed by measuring the strand diameter, pore size in the x-y plane and along the Z direction, as shown in Figures 4.6b and 4.6c, respectively. From the quantitative analysis, it is found that the strand diameter is 565.2 ± 106.4 µm, which is different from the designed diameter due to the printing conditions and swelling property of hydrogels. The pore sizes in the x-y and the y-z direction are 595.7 ± 89.0 µm and 519.7 ± 48.0 µm, respectively. The quantitative analysis results will help with the design of the hydrogel scaffolds.

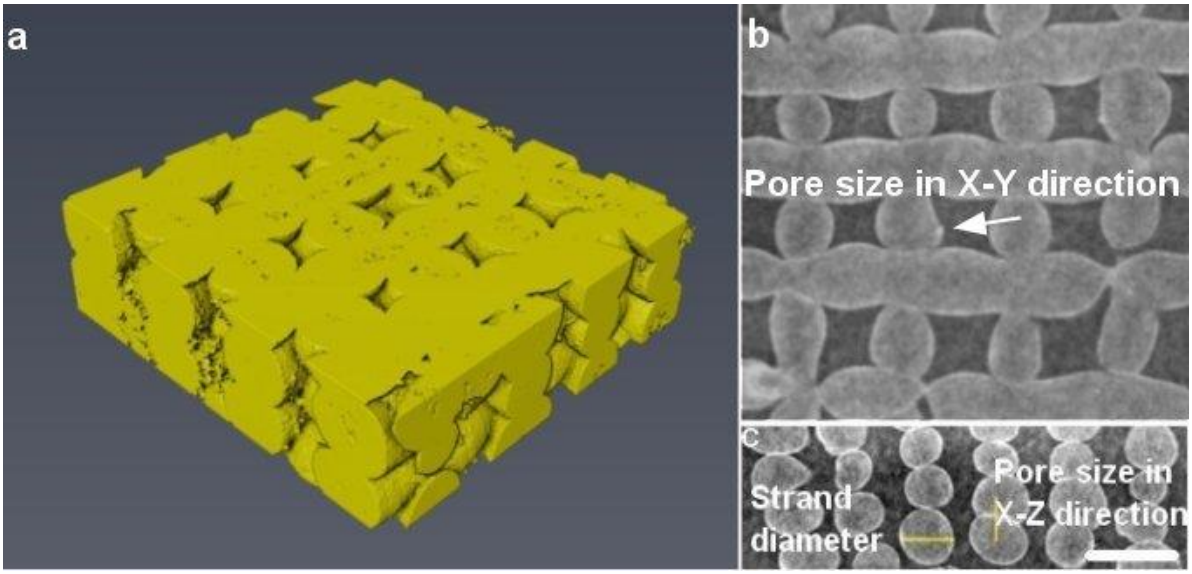

Figure 4.6 3D rendering of a hydrogel scaffold based on the phase retrieval reconstruction images and quantitative measurement according to reconstruction images. (a) 3D rendering model of a hydrogel scaffold; (b) pore size measurement in the X-Y plane; (c) pore size and strand diameter measurement along the Z plane. Scale bar representation indicates 1mm.

4.1.5 Radiation dose reduction using the Paganin-TIE phase retrieval algorithm

The projections captured from the SR-PBI-CT techniques were reconstructed using UFO software. When the projections are reduced from 1800 to 450, to reduce radiation dose during the imaging, the following results are obtained. The results of the phase retrieved reconstructed images with a different number of projections (figure. 4.7d-f), clearly display the hydrogel scaffolds. The intensity profiles (figure. 4.7g-i) of 450, 900, and 1800 projections depict that the reconstructed images of the 450, 900, and 1800 projections can visualize hydrogel scaffolds with reduced radiation dose. The non-phase retrieved images for 450, 900, and 1800 projections (figure. 4.7a-c) again establishes the importance of phase retrieval algorithm in low dose imaging. Because the visualization of hydrogel scaffolds is very challenging or almost invisible in the non-phase retrieved results of 450 and 900 number of projections (figure. 4.7a-b) without the application of Paganin-TIE phase retrieval algorithm. This result shows the effectiveness of the phase retrieval algorithm that support the reduction in radiation exposure of samples by 75% during imaging. The visualization of the hydrogel scaffold is evident in all three different phase retrieved reconstructed images (figure. 4.7d-f). Decreasing the number of projections decreases the radiation dose to the hydrogel scaffold is presented in the given table. 4.1. The reduction in the radiation dose is a significant factor in live animal imaging as a high radiation dose could cause serious injury, even death. The application of phase retrieval algorithm to lower number of projections (900 and 450 projections) still makes hydrogel scaffold structure visible and thus significantly contribute to reduced radiation dose during imaging. This discussion proves that the radiation dose can be significantly reduced by the application of phase retrieval algorithm to lower number of projections. Other factors such as reducing exposure time, and spatial resolution in an acceptable range can also minimize the radiation dose in future studies.

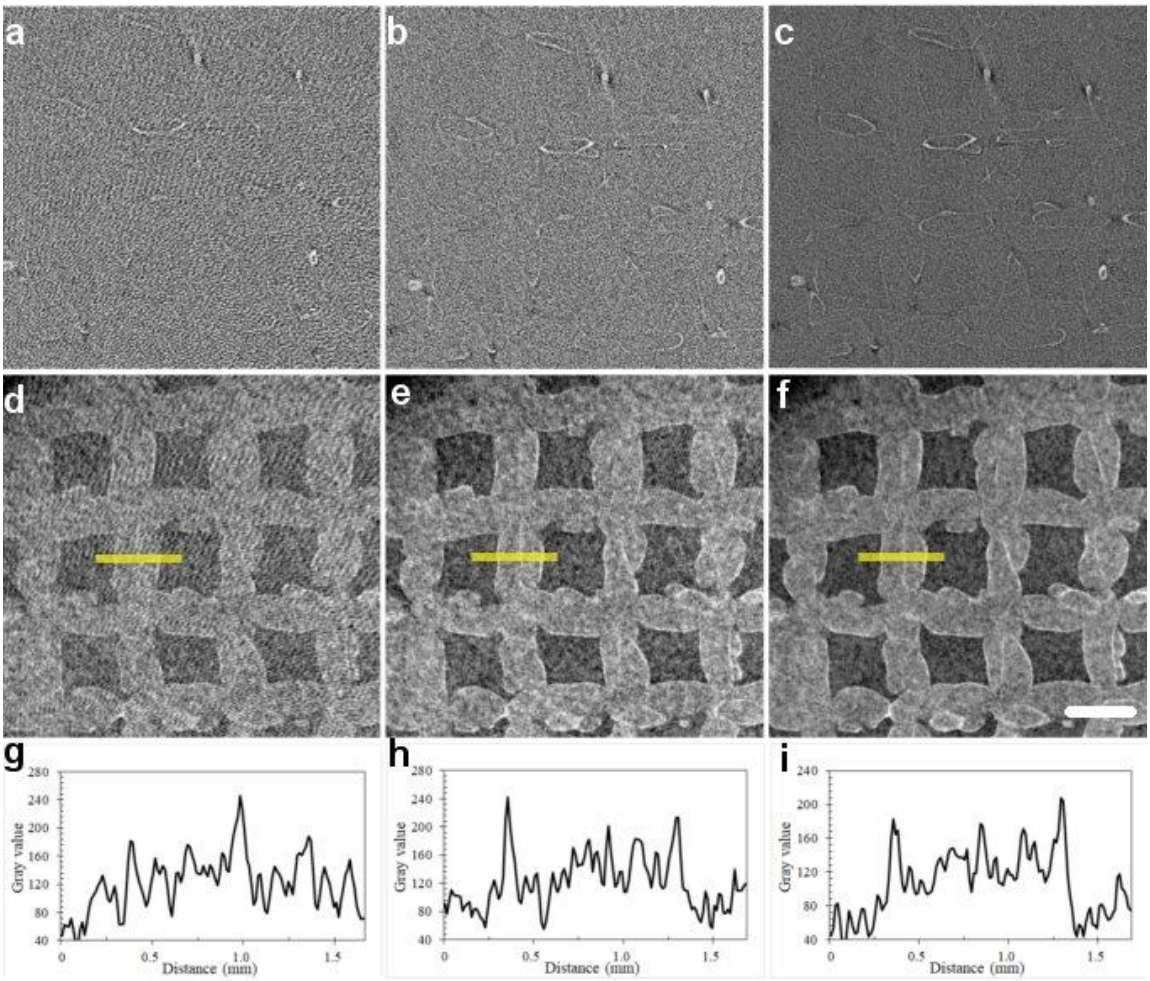

Figure 4.7 Effect of phase retrieval on image quality of low radiation dose reconstruction images. Comparison of non-phase retrieved reconstruction images a) 450 b) 900 c) 1800 and phase retrieved reconstruction images from the CT scan of (d) 450 projections; (e) 900 projections; and (f) 1800 projections. Intensity profiles (g), (h), (i) of the yellow line drawn on phase retrieved images (d), (e), (f). Scale bar indicates 1 mm.

Table 4.1 Effect of the number of projections on radiation dose

Number of projections	Radiation dose (Gy)
450	8.5
900	17.1
1800	34.3

4.2 Hydrogel Scaffold Characterizations using SR-PBI-CT images

4.2.1 Investigation on Printability with different printing speeds of GelMA scaffolds

The printability assessment of hydrogels is very vital to have well-interconnected strands for hydrogel structural integrity with the analysis of strand diameter and pore size in the interconnected network. In general, the interconnected hydrogels are printed in a liquid medium or a supporting print bath. However, the printing of hydrogels in an open-air environment implements various complications such as structural deformation after several layers during printing due to lack of support bath to hold the printed strands. Hence, to obtain well-printed structures of hydrogel scaffolds during printing in a free air surrounding, the examination of printing speed is carried out for GelMA scaffolds printed in an open-air medium.

The images of fabricated hydrogels structures are obtained from the SR-PBI-CT, where the scanning parameters such as SDD and energy are examined for the visualization of hydrogels and to capture images with good contrast and high resolution. The strand details of the scaffolds are visualized from the phase retrieved reconstructed images (figure 4.8), which illustrate the difference in printability with respect to different printing speeds such as 14 mm/s, 16 mm/s, and 18 mm/s. For the quantitative analysis of the printability, the strand diameter and pore size of the hydrogel scaffolds were randomly selected for measurements (Table. 2) (average of nine measurements). The diameter of the GelMA strands at the printing speeds of 14 mm/s, 16 mm/s, and 18 mm/s were 858.7 ± 31.2 µm, 854.2± 48.3 µm, and 503.7 ± 28.3 µm, respectively. The pore sizes of the printed GelMA hydrogels were found to be 1.8 ± 0.1 mm, 2.0 ± 0.1 mm, and 2.4 ± 0.1 mm for 14 mm/s, 16 mm/s, and 18 mm/s of printing speed, respectively. Also, from the phase retrieved reconstructed images (figure 4.8) and quantitative analysis of hydrogel strands, it is clearly seen that increasing the printing speed decreases the strand diameter (figure 4.9a), and so the increase in pore size (figure 4.9b). The unusual change in strand diameter and pore size at 18mm/s is predicted to be the issue of 3D printer reproducibility. The graphical analysis serves as evidence that the printing speed of 18mm/s achieves better printability closely to the designed parameters both in terms of strand diameter printability factor (Ds) and pore size factor (Pxy) as the value of the factors is close to 1 compared to other printing speeds. This quantitative

information from the images indicate that the GelMA hydrogels are printable with suitable printing speed in this case, 18 mm/s, to achieve the designed strand diameter and pore size very closely.

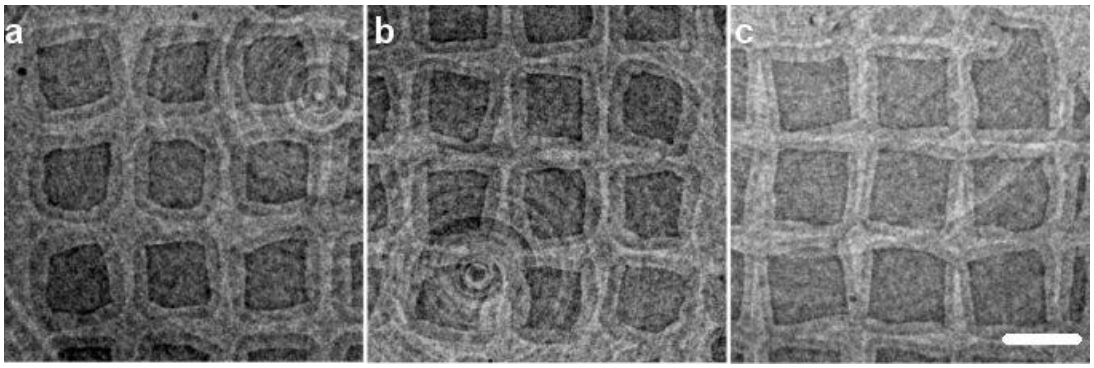

Figure 4.8 Representation of printability with different printing speeds. Comparison of scaffold strands printed at printing speed of (a) 14mm/s; (b) 16mm/s; and (c) 18mm/s. Scale bar indicates 1 mm.

Table 4.2 Quantitative analysis of printability characterization

Printing speed (mm/s)	Measured strand diameter (µm)	Measured pore size in X-Y directions (mm)
14	858.7 ± 31.2	1.8 ± 0.1
16	854.2 ± 48.3	2.0 ± 0.1
18	503.7 ± 28.3	2.4 ± 0.1

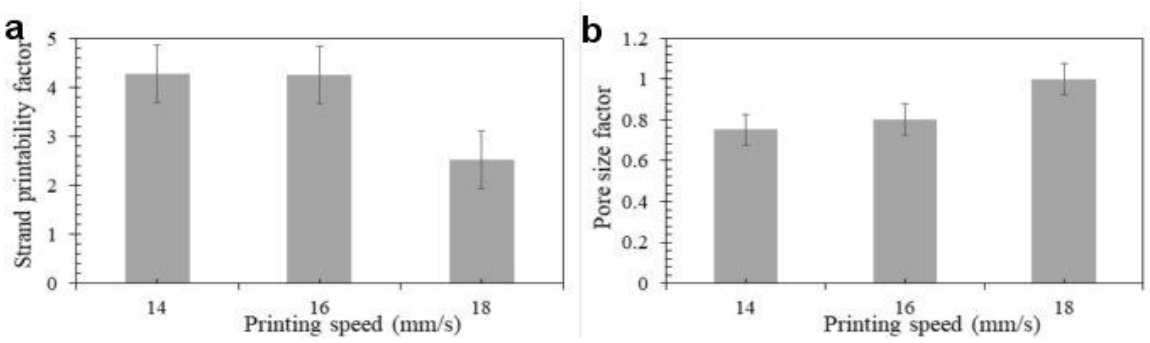

Figure 4.9 Graphical representation of printability factors with different printing speeds. Comparison of (a) strand printability factor and (b) pore size factor with different printing speeds.

4.2.2 Analysis of mechanical deformation of GelMA scaffolds under normal compressions

The characterization of mechanical deformation was performed using SR-PBI-CT technique under various compression levels from 0% to 30%. The variation in the strand diameter and pore size was noticed to characterize the mechanical deformation and to demonstrate that quantitative analysis is phenomenally possible to characterize the mechanical properties when the hydrogel scaffold is experiencing external compressive force. The deformation of scaffolds under various compression levels such as 0%, 10%, 20%, and 30% is shown in (figures 4.10 top view & 4.11 side view). The quantification of pore sizes deformation can be done from the x-y plane or along z plane using the images obtained in either top view or side view, respectively. The obtained results were normalized based on the measured pore size and strand diameter at 0% deformation. The shift in the orientation of the strands along z-direction under intended compression indicates the status of scaffold structure (figure 4.11a-d), with the change in the strand diameter and, as a result, the pore size in the x-y axis is decreased during deformation (figure 4.12b). From the analysis, the mechanical deformation of the GelMA scaffold shows acceptable resistance to external compression and withhold its structural integrity until 20 % compression. But at 30% compression, a little shift is noticed in its strand orientation and it shows no significant shock absorption (figure 4.11d & 4.12a). Because the increase of the strand diameter after 20% deformation (figure. 4.12a) shows no significant change in strand diameter, it indicates that the scaffolds are resistant to absorb the compression (external shock) at 30% deformation. The result confirms the mechanical strength of the scaffolds under different compression levels. Hence, the quantified results predict that the GelMA hydrogel design having 0 - 90˚ inner pattern is strong until 20% compression. Yet it can be further improved since there are no significant shock absorption trends observed at 30% compressions (figure 4.12a), which indicate less shock absorption.

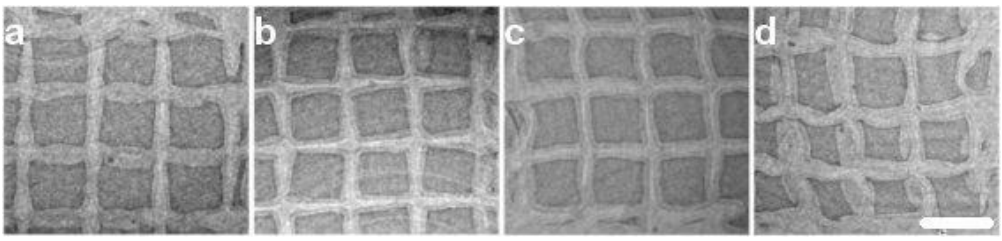

Figure 4.10 Display of hydrogel compression at different levels to analyze pore size in the X-Y direction. Deformation of GelMA scaffolds (Top view) under different levels of normal compressions (a) 0%, (b) 10%, (c) 20%, and (d) 30%. Scale bar representation indicates 1 mm.

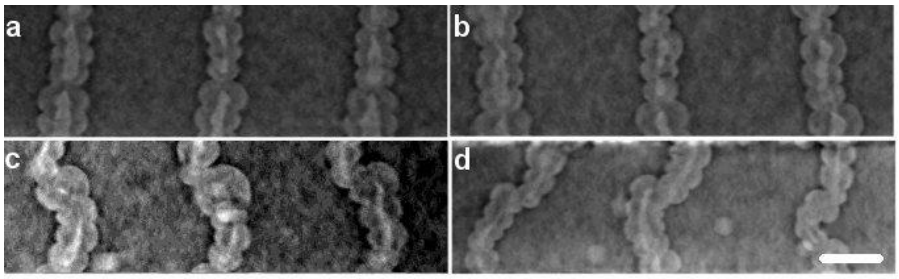

Figure 4.11 Display of hydrogel compression at different levels to analyze pore and strand diameter size in X-Z direction. Deformation of GelMA scaffolds (side view) under different levels of normal compressions (a) 0%, (b) 10%, (c) 20%, and (d) 30%. Scale bar indicates 1 mm.

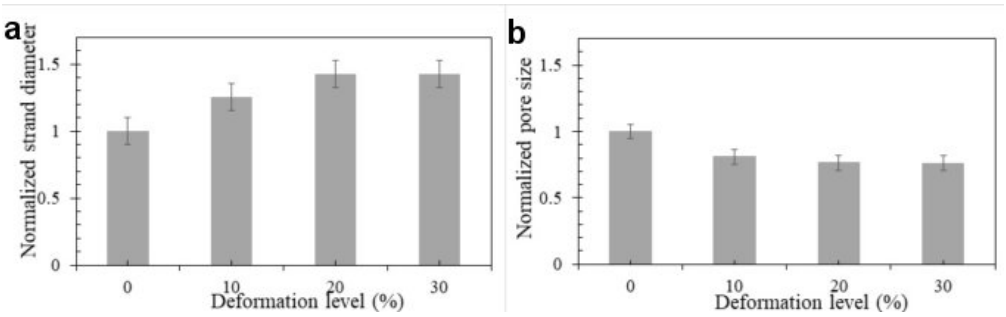

Figure 4.12 Graphical representation of strand diameter and pore size under various compression levels. (a) Normalized strand diameter and (b) Normalized pore size in x-y direction under various deformation levels.

The results significantly display that using the SR-PBI-CT technique to visualize hydrogels under different compressions indicates that this method can be utilized to characterize the mechanical properties of the hydrogel scaffolds in 3D. The advantage of the SR-PBI-CT technique for hydrogel scaffold characterization is explained by calculating the measurement difference between the SR-PBI-CT images with low spatial resolution* (~ 100 µm spatial resolution) which is similar to the spatial resolution of MRI or USI images and the high resolution SR-PBI-CT images (~13 µm spatial resolution). Though the high-resolution MRI or USI imaging modality can reach up to ~ 100 µm spatial resolution which can visualize the hydrogel scaffolds having each strand size of ~ 500 µm, is not suitable to characterize hydrogel scaffolds. From table. 3 it is clearly

evident that the measurement difference obtained between the high- and low-resolution SR-PBI-CT images is very minimal and less than 100 µm, which is impossible to be achieved using the spatial resolution of 100 µm image. Because even using high-resolution MRI or USI having the spatial resolution of ~ 100 µm, it is not possible to visualize and characterize any minimal variations occurring to the sample (e.g. 50 µm). Also, the measurement difference obtained from SR-PBI-CT images between each compression level from 10% to 30% is less than 100 µm, and so MRI or USI cannot be used to characterize the mechanical properties of hydrogel scaffolds having such minimal changes. In addition, using other fabrication techniques (e.g., electrospinning), the hydrogel scaffolds can have each strand diameter of less than 100 µm which cannot be characterized using MRI or USI, even high resolution one. Hence, this research demonstrates that the SR-PBI-CT is the suitable non-destructive imaging technique for hydrogel visualization and has the advantage to characterize the hydrogel scaffolds in both in vitro or in vivo conditions.

Table. 4.3 Measurements difference between the MRI or USI resolution and the SR-PBI-CT resolution

	Low resolution PBI image	**High resolution PBI image**	
Compression level (%)	**Strand diameter (µm)**	**Strand diameter (µm)**	**Difference in measurements (µm)**
0	556 ± 134	503 ± 40	53 ± 94
10	703 ± 130	632 ± 92	71 ± 37
20	758 ± 144	716 ± 95	42 ± 49
30	760 ± 114	719 ± 78	40 ± 36

CHAPTER 5. CONCLUSIONS AND RECOMMENDATIONS

5.1 Summary and Conclusions

Three parts of research work have been carried out and presented in this thesis. The first part of this work is about scaffold fabrication (Alginate scaffold to examine SR-PBI-CT and GelMA scaffolds to characterize printability and mechanical deformation), which was carried out in Biofabrication Laboratory. GelMA was synthesized from Gelatin type A with the addition of Methacrylic anhydride. GelMA has been decided on the interest biomaterial due to its tremendous biomedical applications [33]. The 5% GelMA with 0º - 90º orientation was designed and printed using the 3D Bioplotter. After printing, ultraviolet (UV) light served as a cross-linker during the GelMA scaffold fabrication. It is found that the cross-linking time for the GelMA is 240 seconds, with a distance of 110 mm between the UV light and the sample. Upon printing, the printed scaffolds were stored in the PBS at 4ºC until scanning.

The second part of this research is the study of SR-PBI-CT and different scanning parameters were examined, such as SDD, energy, and number of projections in CT scans. The optimal parameters were found based on the image quality. The third part of this research is to characterize the printed GelMA using the SR-PBI-CT, particularly for the printability and mechanical deformation of the GelMA scaffolds. The last two parts of this research work are carried out at the CLS.

The following conclusions are drawn from the study of SR-PBI-CT for hydrogel imaging and the characterization of printability and deformation of the GelMA scaffolds for their effective use in tissue engineering and regenerative medicine.

The hydrogel scaffolds have been successfully visualized in 3D using the non-destructive SR-PBI-CT technique and demonstrated the applications of this technique in the field of tissue engineering. The advantages of the SR-PBI-CT techniques are higher spatial resolution and better contrast (due to the unique addition of phase contrast) which is practically limited in MRI and USI. The study of SR-PBI-CT by examining different scanning parameters shows the SDD of 150 cm and X-ray energy at 30 keV are recommended to visualize and characterize hydrogel scaffolds with acceptable image quality. Paganin/TIE phase retrieval algorithm has been proved that this

algorithm effectively improves the quality of hydrogel scaffold images. The reduction in the number of projections show the potential of hydrogel scaffold with relatively low in radiation dose and again proves the effectiveness of Paganin/TIE phase retrieval algorithm in hydrogel scaffold imaging. The reported results here mark the effectiveness of propagation-based imaging on hydrogel scaffold visualization compared to conventional absorption-based imaging. The SR-PBI-CT realizes not only 3D visualization of hydrogel scaffolds but also quantitative analysis of scaffold microstructure in 3D. The SR-PBI-CT shows high potentials to be applied in Tissue Engineering and Regenerative Medicine applications (TERM).

Using SR-PBI-CT, the characterization of printed GelMA scaffolds was performed. The printability characterization of GelMA scaffolds showed the higher printing speed of 18 mm/s is the closest printed design to the actual structural design. The results of the mechanical deformation of the GelMA scaffolds showed the scaffold withhold the compression under 20 % deformation without much structural change and showed better external shock absorption compared to 30 % deformation.

Utilization of SR-PBI-CT in quantifying the mechanical properties highlighted the importance of synchrotron imaging techniques in tissue engineering that can not only visualize the 3D structure information but also able to characterize the printability and deformation of scaffolds in a mimicking physiological environment non-destructively. The characterization results will support the design and fabrication of GelMA scaffolds. The novel SR-PBI-CT imaging technique has great potential for non-destructive visualization and monitoring on the status of hydrogel scaffolds after implantation, which is of importance for determining the success of treatments using scaffolds.

The results obtained from this research will benefit the tissue engineering research group for future imaging experiments involving hydrogels at Canadian Light Source to use the SR-PBI-CT technique. Researchers can use the developed holder (Figure) for the mechanical characterization of hydrogel scaffolds since it could mimic the mechanical deformation of hydrogel scaffolds under the physiological environment. The printability assessment and deformation estimation provide researchers with information on the design and fabrication of GelMA scaffolds, and the structural

stability of GelMA scaffolds further to explore their mechanical properties and their tunable characteristics.

5.2 Limitations and recommendations

The limitations of the present research are discussed below, along with the recommendations for future research to address these limitations:

- In the present study, the bioplotter used doesn't have focused UV light, a separate UV block has been utilized and layer-by-layer cross-linking was not carried out because of moving in and out of the UV block, and the stray UV light rays cross-linked the biomaterial ink in the needle present around the printing stage which leads to needle blockage and limited the printing of successive layers. In the future, it would be interesting to develop or incorporate focused UV light for the 3D fabrication of the GelMA scaffold to cross-link in a layer-by-layer fashion during printing. Also, it can focus on controlling the stray light rays from the UV lamp to avoid cross-linking of biomaterial present around the printing stage.

- The printability study was performed with a limited range of printing speed and temperature. Since GelMA is a thermosensitive material, determining the optimal temperature to print GelMA scaffolds could lead to more robust structures. In the present study, the minimum temperature of the printing head was 25^{o}C, and further low temperature printing could be explored to improve printability.

- The imaging was performed with the samples within a water surrounding environment. The results of reducing the radiation dose were achieved by reducing the number of projections by 75 % and can still support qualitative analysis. In the future, similar experiments could be performed *ex vivo* with the scaffolds implanted.

REFERENCES

[1] K. Dzobo *et al.*, "Advances in Regenerative Medicine and Tissue Engineering: Innovation and Transformation of Medicine," *Stem Cells International*, vol. 2018, pp. 1–24, Jul. 2018, doi: 10.1155/2018/2495848.

[2] D. X. B. Chen, *Extrusion Bioprinting of Scaffolds for Tissue Engineering Applications*. Cham: Springer International Publishing, 2019.

[3] K. Y. Lee and D. J. Mooney, "Hydrogels for Tissue Engineering," *Chemical Reviews*, vol. 101, no. 7, pp. 1869–1880, Jul. 2001, doi: 10.1021/cr000108x.

[4] I. M. El-Sherbiny and M. H. Yacoub, "Hydrogel scaffolds for tissue engineering: Progress and challenges," *Global Cardiology Science and Practice*, vol. 2013, no. 3, p. 38, Sep. 2013, doi: 10.5339/gcsp.2013.38.

[5] Y. He, F. Yang, H. Zhao, Q. Gao, B. Xia, and J. Fu, "Research on the printability of hydrogels in 3D bioprinting," *Scientific Reports*, vol. 6, no. 1, p. 29977, Jul. 2016, doi: 10.1038/srep29977.

[6] A. K. Miri, H. G. Hosseinabadi, B. Cecen, S. Hassan, and Y. S. Zhang, "Permeability mapping of gelatin methacryloyl hydrogels," *Acta Biomaterialia*, vol. 77, pp. 38–47, Sep. 2018, doi: 10.1016/j.actbio.2018.07.006.

[7] J. Zhu and R. E. Marchant, "Design properties of hydrogel tissue-engineering scaffolds," *Expert Review of Medical Devices*, vol. 8, no. 5, pp. 607–626, Sep. 2011, doi: 10.1586/erd.11.27.

[8] A. I. van den Bulcke, B. Bogdanov, N. de Rooze, E. H. Schacht, M. Cornelissen, and H. Berghmans, "Structural and Rheological Properties of Methacrylamide Modified Gelatin Hydrogels," *Biomacromolecules*, vol. 1, no. 1, pp. 31–38, Mar. 2000, doi: 10.1021/bm990017d.

[9] S. Y. Nam, L. M. Ricles, L. J. Suggs, and S. Y. Emelianov, "Imaging Strategies for Tissue Engineering Applications," *Tissue Engineering Part B: Reviews*, vol. 21, no. 1, pp. 88–102, Feb. 2015, doi: 10.1089/ten.teb.2014.0180.

[10] A. A. Appel, M. A. Anastasio, J. C. Larson, and E. M. Brey, “Imaging challenges in biomaterials and tissue engineering,” *Biomaterials*, vol. 34, no. 28, pp. 6615–6630, Sep. 2013, doi: 10.1016/j.biomaterials.2013.05.033.

[11] M. Kotecha, “Monitoring Tissue Engineering and Regeneration by Magnetic Resonance Imaging and Spectroscopy,” *Journal of Tissue Science & Engineering*, vol. S11, 2012, doi: 10.4172/2157-7552.S11-007.

[12] I. Georgakoudi, W. L. Rice, M. Hronik-Tupaj, and D. L. Kaplan, “Optical Spectroscopy and Imaging for the Noninvasive Evaluation of Engineered Tissues,” *Tissue Engineering Part B: Reviews*, vol. 14, no. 4, pp. 321–340, Dec. 2008, doi: 10.1089/ten.teb.2008.0248.

[13] M. R. Stacy and A. J. Sinusas, “Emerging Imaging Modalities in Regenerative Medicine,” *Current Pathobiology Reports*, vol. 3, no. 1, pp. 27–36, Mar. 2015, doi: 10.1007/s40139-015-0073-3.

[14] A. Guagliardi, C. Giannini, A. Cedola, M. Mastrogiacomo, M. Ladisa, and R. Cancedda, “Toward the X-Ray Microdiffraction Imaging of Bone and Tissue-Engineered Bone,” *Tissue Engineering Part B: Reviews*, vol. 15, no. 4, pp. 423–442, Dec. 2009, doi: 10.1089/ten.teb.2009.0034.

[15] R. A. Lewis, “Medical phase contrast x-ray imaging: current status and future prospects,” *Physics in Medicine and Biology*, vol. 49, no. 16, pp. 3573–3583, Aug. 2004, doi: 10.1088/0031-9155/49/16/005.

[16] C. J. Gil, M. L. Tomov, A. S. Theus, A. Cetnar, M. Mahmoudi, and V. Serpooshan, “In Vivo Tracking of Tissue Engineered Constructs,” *Micromachines*, vol. 10, no. 7, p. 474, Jul. 2019, doi: 10.3390/mi10070474.

[17] T. Böhm *et al.*, “Quantitative synchrotron X-ray tomography of the material-tissue interface in rat cortex implanted with neural probes,” *Scientific Reports*, vol. 9, no. 1, p. 7646, Dec. 2019, doi: 10.1038/s41598-019-42544-9.

[18] A. Eltom, G. Zhong, and A. Muhammad, “Scaffold Techniques and Designs in Tissue Engineering Functions and Purposes: A Review,” *Advances in Materials Science and Engineering*, vol. 2019, pp. 1–13, Mar. 2019, doi: 10.1155/2019/3429527.

[19] P. Rider, Ž. P. Kačarević, S. Alkildani, S. Retnasingh, and M. Barbeck, “Bioprinting of tissue engineering scaffolds,” *Journal of Tissue Engineering*, vol. 9, p. 204173141880209, Jan. 2018, doi: 10.1177/2041731418802090.

[20] W.-Y. Yeong, C.-K. Chua, K.-F. Leong, and M. Chandrasekaran, “Rapid prototyping in tissue engineering: challenges and potential,” *Trends in Biotechnology*, vol. 22, no. 12, pp. 643–652, Dec. 2004, doi: 10.1016/j.tibtech.2004.10.004.

[21] M. Vukicevic, B. Mosadegh, J. K. Min, and S. H. Little, “Cardiac 3D Printing and its Future Directions,” *JACC: Cardiovascular Imaging*, vol. 10, no. 2, pp. 171–184, Feb. 2017, doi: 10.1016/j.jcmg.2016.12.001.

[22] S. v Murphy and A. Atala, “3D bioprinting of tissues and organs,” *Nature Biotechnology*, vol. 32, no. 8, pp. 773–785, Aug. 2014, doi: 10.1038/nbt.2958.

[23] C. S. Ong *et al.*, “3D and 4D Bioprinting of the Myocardium: Current Approaches, Challenges, and Future Prospects,” *BioMed Research International*, vol. 2018, pp. 1–11, 2018, doi: 10.1155/2018/6497242.

[24] A. Roy, V. Saxena, and L. M. Pandey, “3D printing for cardiovascular tissue engineering: a review,” *Materials Technology*, vol. 33, no. 6, pp. 433–442, May 2018, doi: 10.1080/10667857.2018.1456616.

[25] I. T. Ozbolat and M. Hospodiuk, “Current advances and future perspectives in extrusion-based bioprinting,” *Biomaterials*, vol. 76, pp. 321–343, Jan. 2016, doi: 10.1016/j.biomaterials.2015.10.076.

[26] Y.-J. Choi, H.-G. Yi, S.-W. Kim, and D.-W. Cho, “3D Cell Printed Tissue Analogues: A New Platform for Theranostics,” *Theranostics*, vol. 7, no. 12, pp. 3118–3137, 2017, doi: 10.7150/thno.19396.

[27] S. Naghieh, Md. Sarker, M. Izadifar, and X. Chen, “Dispensing-based bioprinting of mechanically-functional hybrid scaffolds with vessel-like channels for tissue engineering applications – A brief review,” *Journal of the Mechanical Behavior of Biomedical Materials*, vol. 78, pp. 298–314, Feb. 2018, doi: 10.1016/j.jmbbm.2017.11.037.

[28] H. Ding, F. Tourlomousis, and R. C. Chang, “A Methodology for Quantifying Cell Density and Distribution in Multidimensional Bioprinted Gelatin–Alginate Constructs,” *Journal of Manufacturing Science and Engineering*, vol. 140, no. 5, May 2018, doi: 10.1115/1.4037572.

[29] A. D. Olubamiji, Z. Izadifar, N. Zhu, T. Chang, X. Chen, and B. F. Eames, “Using synchrotron radiation inline phase-contrast imaging computed tomography to visualize three-dimensional printed hybrid constructs for cartilage tissue engineering,” *Journal of Synchrotron Radiation*, vol. 23, no. 3, pp. 802–812, 2016.

[30] C. D. Spicer, “Hydrogel scaffolds for tissue engineering: the importance of polymer choice,” *Polymer Chemistry*, vol. 11, no. 2, pp. 184–219, 2020, doi: 10.1039/C9PY01021A.

[31] J. A. Hunt, R. Chen, T. van Veen, and N. Bryan, “Hydrogels for tissue engineering and regenerative medicine,” *J. Mater. Chem. B*, vol. 2, no. 33, pp. 5319–5338, 2014, doi: 10.1039/C4TB00775A.

[32] B. v. Slaughter, S. S. Khurshid, O. Z. Fisher, A. Khademhosseini, and N. A. Peppas, “Hydrogels in Regenerative Medicine,” *Advanced Materials*, vol. 21, no. 32–33, pp. 3307–3329, Sep. 2009, doi: 10.1002/adma.200802106.

[33] K. Yue, G. Trujillo-de Santiago, M. M. Alvarez, A. Tamayol, N. Annabi, and A. Khademhosseini, “Synthesis, properties, and biomedical applications of gelatin methacryloyl (GelMA) hydrogels,” *Biomaterials*, vol. 73, pp. 254–271, Dec. 2015, doi: 10.1016/j.biomaterials.2015.08.045.

[34] R. Kadri *et al.*, “Preparation and characterization of nanofunctionalized alginate/methacrylated gelatin hybrid hydrogels,” *RSC Advances*, vol. 6, no. 33, pp. 27879–27884, 2016, doi: 10.1039/c6ra03699f.

[35] I. Pepelanova, K. Kruppa, T. Scheper, and A. Lavrentieva, “Gelatin-Methacryloyl (GelMA) Hydrogels with Defined Degree of Functionalization as a Versatile Toolkit for 3D Cell Culture and Extrusion Bioprinting,” *Bioengineering*, vol. 5, no. 3, p. 55, Jul. 2018, doi: 10.3390/bioengineering5030055.

[36] K. Yue, G. Trujillo-de Santiago, M. M. Alvarez, A. Tamayol, N. Annabi, and A. Khademhosseini, “Synthesis, properties, and biomedical applications of gelatin methacryloyl (GelMA) hydrogels,” *Biomaterials*, vol. 73, pp. 254–271, Dec. 2015, doi: 10.1016/j.biomaterials.2015.08.045.

[37] H. J. Yoon *et al.*, “Cold water fish gelatin methacryloyl hydrogel for tissue engineering application,” *PLoS ONE*, vol. 11, no. 10, Oct. 2016, doi: 10.1371/journal.pone.0163902.

[38] O. Charles William, *The Scanning Electron Microscope*. London: Cambridge University Press, 1972.

[39] Zhu N, Chen X B, and Chapman D, “A brief review of visualization techniques for nerve tissue engineering,” *Journal of Biomimetics, Biomaterials and Tissue Engineering*, vol. 7, no. 1, pp. 81–99, 2010.

[40] C. Conrad, E. L. Jones, S. D. Newsome, and D. W. Schwartz, “Bone isotopes, eggshell and turkey husbandry at Arroyo Hondo Pueblo,” *Journal of Archaeological Science: Reports*, vol. 10, pp. 566–574, Dec. 2016, doi: 10.1016/j.jasrep.2016.06.016.

[41] I. F. Cengiz, J. M. Oliveira, and R. L. Reis, “Micro-CT – a digital 3D microstructural voyage into scaffolds: a systematic review of the reported methods and results,” *Biomaterials Research*, vol. 22, no. 1, p. 26, Dec. 2018, doi: 10.1186/s40824-018-0136-8.

[42] J. D. Boerckel, D. E. Mason, A. M. McDermott, and E. Alsberg, “Microcomputed tomography: approaches and applications in bioengineering,” *Stem Cell Research & Therapy*, vol. 5, no. 6, p. 144, 2014, doi: 10.1186/scrt534.

[43] *Magnetic Resonance Imaging in Tissue Engineering*. Hoboken, NJ, USA: John Wiley & Sons, Inc., 2017.

[44] M. S. R. Gudur, R. R. Rao, A. W. Peterson, D. J. Caldwell, J. P. Stegemann, and C. X. Deng, "Noninvasive quantification of in vitro osteoblastic differentiation in 3D engineered tissue constructs using spectral ultrasound imaging," *PLoS ONE*, vol. 9, no. 1, pp. 1–10, 2014, doi: 10.1371/journal.pone.0085749.

[45] M. Izadifar, P. Babyn, D. Chapman, M. E. Kelly, and X. Chen, "Potential of propagation-based synchrotron X-ray phase-contrast computed tomography for cardiac tissue engineering," *Journal of Synchrotron Radiation*, vol. 24, no. 4, pp. 842–853, Jul. 2017, doi: 10.1107/S1600577517006208.

[46] A. Momose, T. Takeda, Y. Itai, A. Yoneyama, and K. Hirano, "Perspective for Medical Applications of Phase-Contrast X-Ray Imaging," in *Medical Applications of Synchrotron Radiation*, 1998, pp. 54–62.

[47] F. Pfeiffer, T. Weitkamp, O. Bunk, and C. David, "Phase retrieval and differential phase-contrast imaging with low-brilliance X-ray sources," *Nature Physics*, vol. 2, no. 4, pp. 258–261, Apr. 2006, doi: 10.1038/nphys265.

[48] A. D. Olubamiji, Z. Izadifar, N. Zhu, T. Chang, X. Chen, and B. F. Eames, "Using synchrotron radiation inline phase-contrast imaging computed tomography to visualize three-dimensional printed hybrid constructs for cartilage tissue engineering," *Journal of Synchrotron Radiation*, vol. 23, no. 3, pp. 802–812, May 2016, doi: 10.1107/S1600577516002344.

[49] A. Bravin, P. Coan, and P. Suortti, "X-ray phase-contrast imaging: from pre-clinical applications towards clinics," *Physics in Medicine and Biology*, vol. 58, no. 1, pp. R1–R35, Jan. 2013, doi: 10.1088/0031-9155/58/1/R1.

[50] Y. He, F. Yang, H. Zhao, Q. Gao, B. Xia, and J. Fu, "Research on the printability of hydrogels in 3D bioprinting," *Scientific Reports*, vol. 6, no. 1, p. 29977, Jul. 2016, doi: 10.1038/srep29977.

[51] R. Zehbe, V. H. Schmitt, C. J. Kirkpatrick, and C. Brochhausen, "High resolution X-ray tomography – three-dimensional characterisation of cell–scaffold constructs for cartilage tissue

engineering," *Materials Science and Technology*, vol. 31, no. 2, pp. 167–173, Jan. 2015, doi: 10.1179/1743284714Y.0000000667.

[52] M. Sun, X. Sun, Z. Wang, S. Guo, G. Yu, and H. Yang, "Synthesis and Properties of Gelatin Methacryloyl (GelMA) Hydrogels and Their Recent Applications in Load-Bearing Tissue," *Polymers*, vol. 10, no. 11, p. 1290, Nov. 2018, doi: 10.3390/polym10111290.

[53] J. Yin, M. Yan, Y. Wang, J. Fu, and H. Suo, "3D Bioprinting of Low-Concentration Cell-Laden Gelatin Methacrylate (GelMA) Bioinks with a Two-Step Cross-linking Strategy," *ACS Applied Materials & Interfaces*, vol. 10, no. 8, pp. 6849–6857, Feb. 2018, doi: 10.1021/acsami.7b16059.

[54] S. Naghieh, M. Sarker, N. K. Sharma, Z. Barhoumi, and X. Chen, "Printability of 3D Printed Hydrogel Scaffolds: Influence of Hydrogel Composition and Printing Parameters," *Appl. Sci.*, vol. 10, no. 1, p. 292, Dec. 2019, doi: 10.3390/app10010292.

[55] Vogelgesang, M.; Farago, T.; Morgeneyer, T. F.; Helfen, L.; dos Santos Rolo, T.; Myagotin, A.; Baumbach, T. Real-time image-content-based beamline control for smart 4D X-ray imaging. Journal of synchrotron radiation, Vol. 23, iss. 5, pp. 1254-1263. 2016.

[56] D. Paganin, S. C. Mayo, T. E. Gureyev, P. R. Miller, and S. W. Wilkins, "Simultaneous phase and amplitude extraction from a single defocused image of a homogeneous object," *Journal of Microscopy*, vol. 206, no. 1, pp. 33–40, Apr. 2002, doi: 10.1046/j.1365-2818.2002.01010.x.

[57] P. Baran *et al.*, "Optimization of propagation-based x-ray phase-contrast tomography for breast cancer imaging," *Physics in Medicine and Biology*, vol. 62, no. 6, pp. 2315–2332, Feb. 2017, doi: 10.1088/1361-6560/aa5d3d.

[58] M. C. Strotton *et al.*, "Optimising complementary soft tissue synchrotron X-ray microtomography for reversibly-stained central nervous system samples," *Scientific Reports*, vol. 8, no. 1, Dec. 2018, doi: 10.1038/s41598-018-30520-8.

[59] F. Timischl, "The contrast-to-noise ratio for image quality evaluation in scanning electron microscopy," *Scanning*, vol. 37, no. 1, pp. 54–62, Jan. 2015, doi: 10.1002/sca.21179.

[60] F. Timischl, “The contrast-to-noise ratio for image quality evaluation in scanning electron microscopy,” *Scanning*, vol. 37, no. 1, pp. 54–62, Jan. 2015, doi: 10.1002/sca.21179.

[61] Z. Izadifar, L. Chapman, and X. Chen, “Computed Tomography Diffraction-Enhanced Imaging for In Situ Visualization of Tissue Scaffolds Implanted in Cartilage,” *Tissue Engineering, Part C: Methods*, vol. 20, no. 2, pp. 140–148, 2014.

[62] W. Sun *et al.*, “Experimental Study on Phase-contrast Imaging with Synchrotron Hard X-ray for Repairing Osteonecrosis of the Femoral Head,” *Orthopedics*, vol. 34, no. 9, p. 699, 2011.

[63] A. D. Olubamiji, Z. Izadifar, N. Zhu, T. Chang, X. Chen, and B. F. Eames, “Using synchrotron radiation inline phase-contrast imaging computed tomography to visualize three-dimensional printed hybrid constructs for cartilage tissue engineering,” *Journal of Synchrotron Radiation*, vol. 23, no. 3, pp. 802–812, 2016, doi: 10.1107/S1600577516002344.

[64]. A Snigirev, I. Snigireva, V. Kohn, S. Kuznetsov, and I. Schelokov, “Image formation theory; (100.2960) Image analysis; (110.4980) Partial coherence in imaging,” 1996.

[65] C. Nave, “A comparison of absorption and phase contrast for X-ray imaging of biological cells,” *Journal of Synchrotron Radiation*, vol. 25, no. 5, pp. 1490–1504, Sep. 2018, doi: 10.1107/S1600577518009566.